

**MICROWAVE DRYING OF MINERALS: EXPERIMENTAL AND NUMERICAL  
MODELING**

by

Milad Asgarpour Khansary

B.Sc., University of Tehran, 2011

M.Sc., University of Tehran, 2014

A THESIS SUBMITTED IN PARTIAL FULFILLMENT OF  
THE REQUIREMENTS FOR THE DEGREE OF

MASTER OF APPLIED SCIENCE

in

THE FACULTY OF GRADUATE AND POSTDOCTORAL STUDIES  
(Mining Engineering)

THE UNIVERSITY OF BRITISH COLUMBIA  
(Vancouver)

December 2025

© Milad Asgarpour Khansary, 2025

The following individuals certify that they have read, and recommend to the Faculty of Graduate and Postdoctoral Studies for acceptance, the thesis entitled:

Microwave drying of minerals: experimental and numerical modeling

---

submitted by Milad Asgarpour Khansary in partial fulfilment of the requirements for  
the degree of Master of Applied Science  
in Mining Engineering

---

**Examining Committee:**

Dr. Ali G. Madiseh, Associate Professor, Norman B. Keevil Institute of Mining Engineering,  
UBC  
Supervisor

---

Dr. Marek Pawlik, Professor, Norman B. Keevil Institute of Mining Engineering, UBC  
Supervisory Committee Member

---

Dr. John Thomas Steen, Associate Professor, Norman B. Keevil Institute of Mining  
Engineering, UBC  
Supervisory Committee Member

---

## **Abstract**

This thesis evaluates the application of microwave systems for mineral drying through laboratory experiments and numerical modeling. Four types of minerals were procured from a mining partner, with moisture contents up to 25%. Their material properties – including thermal conductivity, heat capacity, density, initial moisture content, and dielectric loss factor – were characterized. Drying tests were conducted in a commercial microwave oven, with samples exposed to microwave irradiation to reduce moisture content to below 1%, while ensuring temperature control below a specified threshold. Materials were incrementally heated, with mass loss and surface temperature measured until target mass losses were achieved. Results revealed a two-stage drying regime: a constant-rate period up to a critical moisture content, followed by a falling-rate regime.

A numerical replica of the commercial microwave oven was developed, including key components such as three rotating stirrers, a ceramic plate, and three separate magnetrons. Parameters such as air inflow, stirrer rotation speed, microwave generator ramp-up time, and forward power were measured and incorporated into the numerical model. The characterized material properties were integrated into a coupled electromagnetic and heat transfer finite element model implemented in COMSOL Multiphysics to investigate drying rates and temperature profiles. Predicted mass loss and temperature changes under experimental microwave heating conditions were compared with experimental results.

Results indicated that microwave energy was predominantly consumed by water evaporation. For the studied material M2, which contained sulfur and required maintaining temperatures below 125 °C, the numerical model was particularly useful in determining internal temperatures that were experimentally inaccessible. The model predicted maximum material temperatures well below

100 °C during 60 s microwave exposures, sustaining an average drying rate of 2 g/s. These findings demonstrate that microwave heating offers a highly effective alternative for drying applications in mining, particularly where temperature sensitivity is a key operational requirement.

## **Lay Summary**

Microwave energy has shown promise as an efficient method for drying mineral materials, vital for the mining and mineral processing industries. This study explored how minerals with different moisture levels respond to microwave heating. Experiments, using a standard microwave oven, measured moisture reduction and temperature changes throughout the drying process. The results showed a two-stage drying process: a rapid initial moisture loss followed by a slower phase as bound moisture required more energy to release. A numerical simulation model was developed to understand heating dynamics and moisture movement, addressing safety concerns for minerals that could release hazardous gases when overheated. The findings confirmed that microwave drying is effective, with advantages over conventional methods, including shorter processing times, better energy efficiency, and reduced environmental risks. Overall, microwave-assisted drying appears to be a sustainable and effective alternative for mineral drying, enhancing both operational efficiency and environmental performance in mining.

## Preface

The work presented in this dissertation represents the original and independent contribution of its author, Milad Asgarpour Khansary, and was carried out under the guidance of a supervisory panel comprising Dr. Parham Samea, Dr. Amin Shadi, and Dr. Hosein Kalantari, with overall leadership provided by Dr. Ali Madiseh.

The practical component of this research was carried out by the author and involved several stages, beginning with the preparation of mineral specimens for testing. Drying experiments were conducted using a commercially available microwave oven, during which both the reduction in moisture content and the variations in temperature were systematically monitored and documented. Complementary measurements of the thermophysical properties of the minerals, including thermal conductivity and specific heat capacity, were undertaken at McGill University by Dr. Mehrdad Kermani and Dr. Adel Ahmadihosseini.

To enhance the scope of the investigation, the author, together with the supervisory team, developed a computational model designed to simulate the microwave drying process. This model enabled a more comprehensive examination of the heat transfer mechanisms and moisture removal behavior under microwave exposure. For the analytical stage, the author processed the collected experimental data, extracting meaningful trends and correlations regarding the drying responses of different mineral types. The findings of this research highlight the significant potential of microwave technology as an efficient and practical alternative to conventional mineral drying techniques.

Generative AI was not used in any way for any aspect of this work, including its conception, planning, data collection, analysis, writing, or revision.

Three **conference papers** based on the work presented in this thesis has been published.

- i. Milad Asgarpour Khansary, Amin Shadi, Parham Samea, and Seyed Ali Ghoreishi-Madiseh, Experimental Evaluation of Microwave Systems for Minerals Dewatering, COM 2024, Halifax, Nova Scotia, August 1-22, 2024. Published in proceedings of the 63rd Conference of Metallurgists, COM 2024, pp 961–964.
- ii. M. Asgarpour Khansary, H. Kalantari, P. Samea, S.A. Ghoreishi-Madiseh, Microwave Drying of Minerals: Experimental and Numerical Modeling, CIM CONNECT 2025, Montréal, May 4-7, 2025.
- iii. M. Asgarpour Khansary, P. Samea, S.A. Ghoreishi-Madiseh, Microwave Heating for Minerals Drying: Experimental and Numerical Study, the 59th Annual Microwave Power Symposium, Edmonton, June 24-26, 2025.

A version of this thesis has been submitted as a **journal paper**.

- i. Milad Asgarpour Khansary, Parham Samea, and Seyed Ali Ghoreishi-Madiseh. (2025) Microwave Drying of Minerals with Moisture-Dependent Properties: Experimental and Numerical Analysis.

## Table of Contents

<b>Abstract.....</b>	<b>iii</b>
<b>Lay Summary .....</b>	<b>v</b>
<b>Preface.....</b>	<b>vi</b>
<b>Table of Contents .....</b>	<b>viii</b>
<b>List of Tables .....</b>	<b>xi</b>
<b>List of Figures.....</b>	<b>xii</b>
<b>Acknowledgements .....</b>	<b>xvi</b>
<b>Chapter 1: Introduction .....</b>	<b>1</b>
1.1    Motivation.....	2
1.2    Electromagnetic Fundamentals of Microwave Drying .....	4
1.3    The Dielectric Response and Microwave Heating.....	6
1.4    Literature Review and Research Gap .....	7
1.5    Scope of Present Research.....	12
1.6    Chapter Summary .....	13
<b>Chapter 2: Experimental Feasibility Evaluation of Microwave Drying.....</b>	<b>15</b>
2.1    Chapter Introduction .....	16
2.2    Characterization of Material Properties .....	17
2.2.1    Initial Moisture Content.....	17
2.2.2    Density .....	18
2.2.3    Thermal Conductivity .....	19
2.2.4    Heat Capacity.....	20

2.2.5	Electromagnetic Properties .....	21
2.3	Microwave Drying Experiments.....	26
2.3.1	Overall Setup .....	26
2.3.2	Microwave Ramp-up Time and Effective Forward Power.....	27
2.3.3	Microwave Drying Tests.....	28
2.4	Chapter Conclusion.....	34
<b>Chapter 3: Numerical Model Development and Experimental Validation.....</b>		<b>35</b>
3.1	Chapter Introduction .....	36
3.2	Experimental Section .....	38
3.2.1	Detailed Characterization of Material M2 .....	38
3.2.1.1	Initial Moisture Content .....	38
3.2.1.2	Density .....	39
3.2.1.3	Porosity .....	40
3.2.1.4	Thermal Conductivity .....	40
3.2.2	Microwave Drying Tests.....	42
3.2.2.1	Overall Setup .....	42
3.2.2.2	The Microwave Oven .....	43
3.2.2.3	Ramp-up Time .....	44
3.2.2.4	Forward Power.....	45
3.2.2.5	Air inflow.....	46
3.2.2.6	Single-shot Microwave Drying Tests .....	47
3.3	Numerical Section.....	49
3.3.1	Governing Equations .....	49

3.3.2	Initial and Boundary Conditions .....	54
3.3.3	Numerical Stability Considerations .....	54
3.3.4	Model Implementation.....	59
3.3.5	The Quasi-Transient Approach in Solving the Coupled Model .....	60
3.4	Results and Discussion .....	61
3.4.1	Experimental Mass Loss and Temperature .....	61
3.4.2	Effect of Phase Change Interval .....	62
3.4.3	Effect of Thermal Conductivity .....	63
3.4.4	Surface Temperature Profiles: Experimental vs. Numerical .....	65
3.4.5	Heating Uniformity Index.....	69
3.4.6	Power Loss Profile .....	70
3.4.7	Drying Efficiency.....	71
3.4.8	Heat Over Microwave Efficiency (HOME).....	73
3.4.9	Industry-recommended Maximum Temperature Threshold .....	74
3.5	Chapter Conclusion.....	76
<b>Chapter 4: Conclusion</b>	.....	<b>78</b>
4.1	Summary .....	78
4.2	Objectives, Strength and Limitations.....	79
4.3	Possible Future Research Directions .....	80
<b>Bibliography</b>	.....	<b>81</b>

## List of Tables

<b>Table 2.1</b> Measured initial moisture content of as-received samples using overnight hot-air drying.....	18
<b>Table 2.2</b> Measured density of samples.....	18
<b>Table 2.3</b> Measured thermal conductivity of as-received and fully dried samples.....	19
<b>Table 2.4</b> Fitting parameters evaluated for the linearity relationship for the samples at a frequency of 2.45 GHz.....	25
<b>Table 2.5</b> Effect of microwave energy dosages on moisture loss.....	34
<b>Table 3.1</b> Initial moisture measurement of material M2.....	38
<b>Table 3.2</b> Measured airflow into the cavity through two rectangular meshed entrances using an anemometer.....	47
<b>Table 3.3</b> The details of microwave drying experiment.....	48
<b>Table 3.4</b> The calculated values of forced convection coefficient applied to lateral surfaces of the sample.....	53
<b>Table 3.5</b> Measured surface temperature and water removed at each microwave dosage.....	62
<b>Table 3.6</b> The effect of prescribed phase change interval on predicted mass loss.....	63
<b>Table 3.7</b> Surface temperature measured using IR camera thermal imaging, with corresponding numerical predictions (in parenthesis).....	67

## List of Figures

<b>Figure 2.1</b> Samples procured from a partner mining company.....	16
<b>Figure 2.2:</b> (a) The hot-air blown oven used to measure initial moisture content, and (b) sample (M2) after 24hrs of drying. ....	17
<b>Figure 2.3</b> Heat capacity measurements for four type of minerals. ....	20
<b>Figure 2.4</b> Cavity perturbation setup (a) together with (b) schematic of parts and (c) a close look at sample holder. ....	21
<b>Figure 2.5</b> Measured tangent loss of M1 at 5 different frequencies using cavity perturbation technique.....	22
<b>Figure 2.6</b> Measured tangent loss of M2 at 5 different frequencies using cavity perturbation technique.....	23
<b>Figure 2.7</b> Measured tangent loss of M3 at 5 different frequencies using cavity perturbation technique.....	23
<b>Figure 2.8</b> Measured tangent loss of M4 at 5 different frequencies using cavity perturbation technique.....	24
<b>Figure 2.9</b> The linearity relationship between $\epsilon''/\rho$ and $\epsilon'/\rho$ for the samples at a frequency of 2.45 GHz.....	25
<b>Figure 2.10</b> Experimental setup showing a 3kW microwave oven, benchtop scale and an IR thermal camera.....	26
<b>Figure 2.11</b> Measured load energy absorption for ramp-up time of the microwave oven.....	27
<b>Figure 2.12</b> Measured changes in maximum surface temperature for M1 (shaded area shows the datapoints collected during cooling – outside microwave cavity).....	29

<b>Figure 2.13</b> Measured changes in maximum surface temperature for M2 (shaded area shows the datapoints collected during cooling – outside microwave cavity).....	29
<b>Figure 2.14</b> Measured changes in maximum surface temperature for M3 (shaded area shows the datapoints collected during cooling – outside microwave cavity).....	30
<b>Figure 2.15</b> Measured changes in maximum surface temperature for M4 (shaded area shows the datapoints collected during cooling – outside microwave cavity).....	30
<b>Figure 2.16</b> Measured changes in mass for M1.....	31
<b>Figure 2.17</b> Measured changes in mass for M2.....	32
<b>Figure 2.18</b> Measured changes in mass for M3.....	32
<b>Figure 2.19</b> Measured changes in mass for M4.....	33
<b>Figure 3.1</b> Measured densities of wet, dry and solid (pore-free) material M2.....	40
<b>Figure 3.2</b> Nominal thermal conductivity of the material determined using the geometric mean model.....	41
<b>Figure 3.3</b> Full experimental setup used to perform microwave drying tests.....	43
<b>Figure 3.4</b> Measured ramp-up time using thermal energy absorbed by 140 g of water at different exposure times.....	45
<b>Figure 3.5</b> Measured forward power.....	46
<b>Figure 3.6</b> Mesh dependency analysis of resistive power loss and heat power balance with dashed trendlines.....	57
<b>Figure 3.7</b> The number of elements (degree of freedom) generated with mesh refinement and their respective computational costs (measured for ten consecutive iterations), with dashed trendlines.....	57

<b>Figure 3.8</b> The <i>h</i> -convergence analysis for electromagnetic and heat transfer meshes, illustrating error reduction with mesh refinement.....	58
<b>Figure 3.9</b> Schematic representation of the modelled microwave oven illustrating: (a) its components including mode stirrers (highlighted in yellow), the ceramic support plate (highlighted in red), and the sample (highlighted in green); and (b) the finite element mesh used for electromagnetic and heat transfer simulations. ....	59
<b>Figure 3.10</b> Convergence of power loss averaged over discrete angular positions for a single revolution.....	61
<b>Figure 3.11</b> Dependency of numerical results for evaporation on the thermal conductivity (with $\Delta T = 2.5 \text{ } ^\circ\text{C}$ ).....	64
<b>Figure 3.12</b> Failure of arithmetic mean thermal conductivity model in prediction of evaporation (with $\Delta T = 2.5 \text{ } ^\circ\text{C}$ ). ....	65
<b>Figure 3.13</b> Comparison of the average surface temperature recorded by an IR Camera with numerical model predictions for Cases I through V. Numerical results for $\Delta T = 2.5 \text{ } ^\circ\text{C}$ and $k_s = 1.79 \text{ W m}^{-1} \text{ K}^{-1}$ .....	66
<b>Figure 3.14</b> Comparison of the surface temperature profiles captured by IR imaging (left) with numerical results (right) for Cases I through III. ....	68
<b>Figure 3.15</b> Comparison of uniformity index for Cases I through V. Numerical results for $\Delta T = 2.5 \text{ } ^\circ\text{C}$ and $k_s = 1.79 \text{ W m}^{-1} \text{ K}^{-1}$ .....	69
<b>Figure 3.16</b> The computed resistive power loss (Numerical results for $\Delta T = 2.5 \text{ } ^\circ\text{C}$ and $k_s = 1.79 \text{ W m}^{-1} \text{ K}^{-1}$ ).....	70
<b>Figure 3.17</b> Comparing the experimental and numerical drying efficiency. Numerical results for $\Delta T = 2.5 \text{ } ^\circ\text{C}$ and $k_s = 1.79 \text{ W m}^{-1} \text{ K}^{-1}$ .....	72

**Figure 3.18** The computed heat over microwave efficiency (Numerical results for phase change interval  $\Delta T = 2.5 \text{ } ^\circ\text{C}$  and  $k_s = 1.79 \text{ Wm. K}$ ) ..... 73

**Figure 3.19** Maximum volume temperatures. Numerical results for  $\Delta T = 2.5 \text{ } ^\circ\text{C}$  and  $k_s = 1.79 \text{ Wm. K}$  ..... 75

**Figure 3.20** Comparison of maximum surface and volume temperatures. Numerical results for  $\Delta T = 2.5 \text{ } ^\circ\text{C}$  and  $k_s = 1.79 \text{ Wm. K}$  ..... 75

## **Acknowledgements**

I would like to express my sincere gratitude to Dr. A. G. Madiseh, Dr. P. Samea, Dr. A. Shadi, and Dr. H. Kalantari for their continuous guidance, encouragement, and support throughout this journey.

Part of this work was undertaken in close collaboration with Dr. Ferri Hassani's research group, and special acknowledgment is extended to Dr. Mehrdad Kermani and Dr. Adel Ahmadihosseini for their invaluable assistance in performing the experimental procedures.

This research was supported by the Mitacs Accelerate Program and the CleanBC Industry Fund. The computations in this research were supported in part through the computational resources and services provided by Advanced Research Computing (ARC Sockeye Systems) at the University of British Columbia as well as Digital Research Alliance of Canada (the Alliance).

## **Chapter 1: Introduction**

In this chapter, an overview of the research conducted in this thesis is presented, along with its underlying motivations and the identified gaps in the literature. The rationale for retrofitting/hybridizing the conventional drying operations with microwave-based heating, as well as its practical applicability, is introduced. A thorough literature review is provided, focusing on studies related to microwave drying of minerals, and highlighting the key challenges associated with modeling such processes.

## 1.1 Motivation

The mining industry is recognized as a major source of greenhouse gas emissions, making it a key focus in global efforts to reduce environmental impacts [1]. To align with sustainability targets, this sector faces growing pressure to transition away from conventional, fossil fuel-dependent practices and adopt cleaner, more efficient alternatives. One critical operation in mining that demands attention is mineral drying, which has traditionally been powered by coal, diesel, or natural gas. These fuel-intensive methods not only consume large amounts of energy but also release significant quantities of carbon dioxide and other pollutants into the atmosphere. In addition to carbon emissions, the combustion process generates harmful byproducts such as nitrogen oxides ( $\text{NO}_x$ ) and sulfur dioxide ( $\text{SO}_2$ ), both of which contribute to air quality degradation and environmental challenges like acid rain [2]. As a result, exploring innovative drying technologies that can reduce reliance on fossil fuels is essential for minimizing the industry's ecological footprint while maintaining productivity.

Reducing the mining sector's reliance on energy-intensive systems is essential for tackling the issues of excessive fuel consumption, heightened greenhouse gas output, and the release of harmful emissions [3]. To achieve this, operators are encouraged to implement advanced technologies that emphasize energy efficiency while modernizing their mineral drying practices. The potential environmental gains from such improvements are significant. For instance, upgrading the drying infrastructure of just one mining operation has been estimated to cut greenhouse gas emissions by approximately 26,000 tonnes of carbon dioxide equivalent. This reduction is comparable to eliminating the combustion of nearly 36 million cubic meters of natural gas, highlighting the scale of impact that targeted retrofits can deliver. Beyond lowering emissions, these interventions can

also help companies stabilize operating costs, improve compliance with tightening environmental regulations, and strengthen their long-term sustainability performance.

Transitioning mineral drying systems away from fossil fuel combustion and toward renewable power sources—such as hydroelectricity—offers the mining industry a direct pathway to cutting its carbon footprint [4, 5]. This shift, commonly referred to as electrification, represents more than just a substitution of energy inputs. By replacing fuels like natural gas with clean electricity, mining companies can reduce their exposure to volatile fuel prices, avoid the financial burden of rising carbon taxes, and benefit from comparatively lower electricity costs. At the same time, electrification delivers substantial environmental advantages by sharply reducing greenhouse gas emissions and associated pollutants [6]. In addition to these immediate benefits, the adoption of renewable-powered drying systems also aligns with broader global sustainability objectives, strengthens a company’s social license to operate, and positions the sector as a proactive player in the transition to a low-carbon economy.

Microwave-based heating technologies are increasingly recognized as being consistent with the broader objective of lowering greenhouse gas emissions and advancing toward an electricity-driven, sustainable energy system [7]. As an alternative to fossil fuel–powered drying methods, microwave heating offers a highly efficient and environmentally responsible solution, with studies indicating that it can be at least twice as effective as conventional approaches [8]. The underlying advantage of this method lies in the way energy is delivered to the material. Traditional drying systems typically rely on conduction and convection, which often result in significant thermal losses and uneven heating of the mineral bed. In contrast, microwaves penetrate the material and interact primarily with water molecules, since most minerals are relatively transparent to microwave radiation [9-14]. This selective absorption means that energy is focused on evaporating

moisture rather than unnecessarily heating the entire solid mass. As a result, drying proceeds more rapidly, with less risk of overheating at the material surface. By overcoming the inefficiencies of conduction-based heat transfer, microwave drying ensures better control, higher energy utilization, and improved product quality [10].

## 1.2 Electromagnetic Fundamentals of Microwave Drying

Microwaves are a form of electromagnetic radiation situated within the radiofrequency region of the electromagnetic spectrum [15]. They occupy wavelengths ranging from approximately 1 mm to 1 m, corresponding to frequencies between 300 MHz and 300 GHz. For industrial and laboratory heating applications, including drying, the most commonly used frequency is 2.45 GHz, which corresponds to a wavelength of about 12.24 cm. This frequency is selected internationally to avoid interference with communication systems while still allowing efficient coupling of electromagnetic energy into water and other polar materials.

In microwave heating, energy transfer occurs through the interaction between the oscillating electromagnetic field and polar molecules—primarily water—within the material [16]. When subjected to the alternating electric field, these molecules attempt to align with the rapidly changing field direction. The continual rotation and friction generated at the molecular level lead to dielectric heating, which results in volumetric temperature rise throughout the material. This differs fundamentally from conventional heating, where heat is transferred from the surface inward through conduction. Because microwaves deposit energy directly inside the sample, heating tends to be faster and more spatially distributed, though it may also lead to thermal gradients and localized overheating if not properly controlled [17].

Within microwave cavities—whether domestic ovens, laboratory reactors, or industrial dryers—the electromagnetic field distribution plays a crucial role in determining heating uniformity. Cavities often include components such as mode stirrers or moving trays to continuously alter the field pattern and reduce the formation of standing-wave “hot spots” [17]. As the material absorbs energy, moisture begins to vaporize, and the internal pressure gradient drives the vapor toward the surface. This volumetric heating accelerates moisture migration compared with conventional drying methods, enabling higher drying rates and shorter processing times. However, the non-uniform nature of microwave fields, differences in dielectric properties, and changes in moisture content during drying can lead to complex interactions, potentially causing overheating or uneven drying if not properly managed.

Overall, microwave drying leverages the unique position of microwaves in the electromagnetic spectrum and the dielectric response of materials to achieve rapid and energy-efficient moisture removal, while also presenting challenges in process control, cavity design, and thermal uniformity. Commercial implementation of microwave heating for mineral drying faces several significant technical, operational, and economic challenges [18].

From an engineering perspective, scaling microwave systems from the laboratory to industrial throughputs is difficult due to limited penetration depth [19]. At 2.45 GHz, microwave penetration depth can be only a few centimeters for many mineral materials. This restricts the effective sample thickness that can be heated volumetrically and necessitates the use of thin layers, moving beds, or hybrid systems. The design of large industrial microwave cavities also becomes challenging because maintaining a uniform electromagnetic field distribution over large volumes is difficult, even with mode stirrers or conveyor systems.

The economics of large-scale microwave drying remained a barrier. Microwave generators and high-power magnetrons or solid-state sources are relatively expensive, and the overall energy cost per tonne of product can exceed that of conventional thermal dryers unless the process yields substantial efficiency gains or product-quality benefits. Maintenance requirements, equipment lifespan, and the need for electromagnetic shielding further contribute to capital and operational costs. Other operational challenges include the need for robust high-temperature materials for cavity linings, waveguides, and components exposed to dust, abrasion, and corrosive environments typical of mineral processing. The presence of conductive minerals (e.g., magnetite, sulfides) also introduces additional complications, as these materials can reflect microwaves or lead to arcing and plasma formation when improperly managed [19].

### **1.3 The Dielectric Response and Microwave Heating**

One method commonly used to evaluate how a material responds to microwave exposure is by examining its dielectric loss factor ( $\epsilon''$ ) [11, 20]. This parameter provides insight into the material's ability to absorb and dissipate electromagnetic energy as heat. Substances with very high dielectric loss, such as metals, tend to reflect most of the incident microwave radiation rather than absorb it. In these cases, the penetration depth approaches zero, preventing microwaves from effectively transmitting into the bulk of the material. At the opposite extreme, materials with extremely low dielectric loss factors—such as quartz or alumina—allow microwaves to pass through with little interaction, resulting in minimal heating. For both of these categories, conventional thermal methods are generally more efficient than microwave-assisted drying [21]. However, materials that fall between these two extremes exhibit more favorable characteristics for microwave processing. Examples include moist minerals and water-containing systems, where the dielectric

properties enable efficient absorption of microwave energy. This makes microwave irradiation particularly advantageous for accelerating heating and drying in such cases, as the energy is selectively targeted toward the moisture content rather than the entire solid matrix.

#### 1.4 Literature Review and Research Gap

Microwave-assisted drying has attracted considerable attention as a promising technique and has been the subject of extensive research using both experimental studies and numerical modeling approaches. A wide range of raw materials and industrial products have been examined under microwave irradiation, highlighting its versatility across different sectors. For example, investigations have been carried out on fossil-based resources such as coal [22-29] and lignite [30-33], as well as on mineral ores including chalcopyrite [34], zinc oxide–sulfide ores [35], manganese ore [36], and zirconia [37]. Additional studies have focused on non-metallic minerals and industrial byproducts such as kaolin clay [38], sand [39], glass [40], vanadium slag [41], and steel-slag–asphalt composites [42]. These diverse applications demonstrate the broad potential of microwave heating as an alternative drying method, offering energy efficiency and selective heating benefits across a spectrum of material types.

In much of the existing literature, numerical modeling has primarily been employed as a supporting tool to confirm experimental observations, particularly for evaluating variations in temperature and mass loss in relatively thin samples. While this approach is useful, its value becomes even more pronounced when dealing with thermally sensitive materials such as sulfur-bearing minerals [43]. For these systems, direct experimental measurements of internal temperature gradients are extremely difficult—often impossible—due to the risk of altering or damaging the sample during

testing. Even in comparatively less complex systems, like liquids or gels, obtaining accurate in-situ temperature profiles remains a major challenge [44].

Numerical simulations therefore provide a critical alternative, offering detailed insights into heat and mass transfer behaviors that are otherwise inaccessible. By constructing robust and validated computational models, it becomes possible to design effective control strategies for the drying process of sulfur-rich ores. Such models can guide decisions regarding optimal energy input, irradiation duration, and exposure conditions, ultimately ensuring efficient drying while avoiding localized overheating or undesirable chemical transformations.

A substantial body of research has focused on the numerical modeling of microwave-assisted heating and drying. Although these models are often highly sophisticated, their practical application has been hindered by the limited availability of reliable transport properties—such as permeability, diffusivity, and moisture conductivity. In many cases, these parameters must be assumed or arbitrarily assigned due to experimental challenges, uncertainties, and the lack of systematic characterization techniques.

Early modeling efforts attempted to capture the coupled mechanisms of heat, mass, and electromagnetic energy transfer in porous materials. For instance, Turner and Jolly [14] developed models to describe drying in non-hygroscopic systems such as brick. Their work emphasized the critical role of pressure build-up within the porous network [45, 46] and introduced the concept of a "pumping effect", where internal gradients in temperature and pressure drive liquid water toward the surface. This phenomenon was later confirmed experimentally in the microwave drying of lignite spheres by Fu et al. [31]. Turner and Jolly [14] also suggested that microwave irradiation is most effective when applied during the initial stages of drying, acting as a pre-treatment step rather than as a late-stage drying method [38, 47].

Building on these foundations, Constant et al. [48] highlighted the necessity of incorporating appropriate boundary conditions for surface mass transfer to correctly describe evaporation kinetics. Instead of directly coupling electromagnetic fields to heat and mass balances, their approach relied on measuring reflected and residual powers with an HF milliwattmeter and then applying a linear relationship between dissipated power and moisture content in the wet phase. Later improvements were made by Hassini et al. [49], who refined the dissipation term by accounting for the dry fraction of the material and by implementing interfacial fluxes driven by internal gas pressure gradients. Similarly, Kumar et al. [50] extended this framework by embedding moisture fluxes directly into heat transfer boundary conditions, thereby representing energy losses linked to surface evaporation.

The influence of microstructural characteristics on drying kinetics has also been explored. Properties such as porosity, pore-filling agents, binder distribution [39, 40], water type (surface and pore moisture) [51], phase composition [52], particle or sample size [53], and even chemical reactions occurring during heating [54] have all been shown to strongly influence both pressure dynamics and drying rates. Huang et al. [22] developed a finite-element model in COMSOL that explicitly coupled electromagnetic, thermal, and moisture transport processes in coal. However, due to the absence of accurate input data, critical parameters such as moisture diffusivity and transfer coefficients still had to be estimated. Comparable limitations have been reported in the works of Hong et al. [55], Li et al. [56], and Montienthong et al. [57], where temperature- and moisture-dependent thermophysical properties (e.g., dielectric constant, specific heat, or conductivity) were not fully incorporated into the simulations. Si et al. [30], for example, were required to assume hydrodynamic and thermal coefficients to reproduce lignite drying rates in their coupled model.

Kowalski et al. [58] experimentally studied kaolin drying and developed a three-phase numerical framework. Their study underscored that the most significant bottleneck in predictive modeling lies in accurately determining transport properties. Achieving this often demands extensive experimental campaigns, specialized equipment, and expert handling, making large-scale implementation of such models particularly challenging.

Despite significant advances in the development of coupled transport and momentum equations, even models supported by accurate empirical transport coefficients and correlations have struggled to reproduce the full complexity of microwave-assisted drying. Two central issues account for these limitations: (1) the omission of temperature- and moisture-dependent material properties [59], and (2) the inadequacy of traditional flow representations based on the Navier–Stokes framework. The latter arises because microwave irradiation induces fluctuations (time derivatives of the fields) in electromagnetic and thermal fields at nanometer or even sub-nanometer scales, well below the spatial resolution where continuum mechanics assumptions remain valid [60-62]. In fact, the flow models such as Navier–Stokes equations can only provide a meaningful approximation when the discretization length in a simulation is several times larger—typically at least sixfold—than the characteristic size of the physical heterogeneities within the material [60-62]. To overcome these limitations of flow models, it has been suggested that conventional fluid flow models must be augmented with the Maxwell stress tensor, which accounts for volumetric electric forces acting on the material. These forces can be expressed as the combined contributions of Coulomb ( $\rho_f E$ ), dielectrophoresis ( $\frac{\varepsilon_0 E^2}{2} \nabla \varepsilon_r$ ) and electrostriction ( $\frac{1}{2} \varepsilon_0 \nabla(bE^2)$ ) forces [63-65].

The relative importance of these mechanisms depends strongly on the local strength and distribution of the electric field. However, the inclusion of dielectrophoresis and electrostriction

has been largely avoided in the literature, primarily because of the significant computational overhead and the difficulty of obtaining the necessary input parameters. For example, accurately resolving spatial variations in dielectric permittivity ( $\epsilon_r$ ) requires either high-precision experimental methods, such as electrostatic force microscopy, or advanced first-principles simulations such as ab initio calculations [66-68]. Both approaches are typically restricted to small-scale samples, making their application to larger, heterogeneous systems impractical [69]. Given these challenges, the incorporation of such effects is often considered unjustifiable in applied modeling studies. Consequently, this work—similar to most prior studies—does not pursue the inclusion of these contributions, focusing instead on more tractable formulations that balance computational feasibility with predictive accuracy.

The dependency of material properties on moisture content and/or temperature, along with their accurate characterization and implementation in numerical models, is recognized as a pivotal factor in predicting the thermal response of materials subjected to microwave energy inputs [10]. Conventional approaches often assume constant values for key thermophysical and dielectric parameters such as specific heat capacity, thermal conductivity, and dielectric constant. However, experimental evidence and theoretical considerations suggest that these properties vary significantly as a function of the evolving moisture distribution and the rising temperature within the sample [70-73]. For example, the dielectric constant of water, which dominates the absorption of microwave radiation in moist materials, decreases with increasing temperature, thereby altering the penetration depth and distribution of absorbed energy.

Failure to capture these coupled dependencies pose as a major shortcoming of earlier modeling efforts, leading to discrepancies between simulated and observed drying kinetics. This issue becomes particularly acute for thermally sensitive matrices such as sulfur-bearing ores, where

localized overheating or incomplete drying can have critical consequences for both material stability and process efficiency. Robust characterization of moisture- and temperature-dependent properties therefore remains a cornerstone for developing predictive models. A rigorous implementation of these variable properties would not only improve the fidelity of thermal response predictions but also allow for the design of more effective control strategies. For instance, by accounting for the dynamic decrease in dielectric loss with moisture depletion, models could help optimize irradiation time and energy dosage, preventing unnecessary energy input at later drying stages where microwave absorption becomes inefficient [74].

## 1.5 Scope of Present Research

This study was designed to evaluate microwave heating as a practical and energy-efficient alternative for mineral drying processes. A thorough characterization of the mineral samples was performed prior to experimentation, including measurements of thermal conductivity, specific heat capacity, moisture content, bulk density, and dielectric properties, particularly the dielectric loss factor, which governs the absorption of microwave energy. These parameters provided a foundational understanding of how the materials would respond to electromagnetic irradiation.

Drying experiments were conducted using a commercial microwave oven, which was first carefully calibrated to assess its power ramp-up behavior and to accurately determine the forward power delivered to the samples. This step was critical to ensure reproducibility and reliability in the experimental data.

Complementing the empirical work, a finite element model was constructed to simulate the coupled electromagnetic and thermal responses during microwave heating. The model accounted for the energy deposition within the mineral samples, incorporating their measured dielectric and

thermal properties to predict temperature evolution and moisture removal over time. By systematically comparing the numerical predictions with the experimental results, the study aimed to validate the model's accuracy and identify potential deviations arising from simplifying assumptions or unaccounted material behaviors. This combined experimental–numerical approach provided a comprehensive framework for understanding microwave-assisted drying and offered insights into optimizing process parameters for different types of mineral samples.

## 1.6 Chapter Summary

Drying is a major unit operation in mining. Currently, rotary dryers are widely used for this purpose. They consume huge amounts of natural gas, and produce significant greenhouse gas emissions. With rising carbon taxes, this becomes a major cost. On the other hand, there is also operational challenges, such as: insufficient control over material temperature, the possibility of toxic gas emission and flames / ignition. Therefore, there's a motivation to look for more cleaner technologies.

- In this work, microwave heating is proposed and investigated as an alternative, because water absorbs microwave energy far stronger than most minerals. In other words, most of energy should go to water evaporation rather than heating of the solid.

The most significant limitations identified in previous studies can be grouped into both experimental and numerical shortcomings.

- i. Experimentally, very few works have examined the potential risks associated with toxic gas release during processing, and overheating phenomena were often neither monitored nor reported. In addition, the occurrence of oxidation and possible ignition was not

adequately addressed, and most investigations lacked proper characterization and inspection of the microwave cavity.

- ii. From a numerical perspective, existing models frequently failed to capture the full Multiphysics nature of the problem and did not sufficiently integrate experimentally derived material characterization data. Furthermore, transient modeling of mode stirrers—representing the dynamic behavior of moving components within the cavity—remains immature and underdeveloped. Together, these limitations highlight the need for more comprehensive, well-integrated experimental and numerical approaches.

In this study, we aim to address several key research questions related to the microwave-assisted drying process. Specifically, we investigate:

- i. How temperature and moisture content evolve under varying microwave energy dosages and whether overheating phenomena emerge at higher power levels.
- ii. A central objective is to evaluate how moisture removal rates change with different energy inputs and to determine the feasibility of achieving target moisture reduction levels while remaining below industry-recommended temperature thresholds.
- iii. In parallel, we seek to develop and validate a numerical model capable of capturing the essential thermal and moisture transport behaviour. The model is intended to be sufficiently simple to remain computationally affordable, yet robust and reliable enough to predict experimental observations and guide the design and optimization of microwave drying systems.

## **Chapter 2: Experimental Feasibility Evaluation of Microwave Drying**

The primary objective of this chapter was to evaluate the practicality of using microwave heating to reduce the moisture content of mineral samples to their target levels, specifically below 1%. The chapter outlines the full process, including sample procurement, characterization techniques, experimental setup, and procedural steps, for four distinct types of mineral samples provided by a mining partner company. Each material was systematically characterized to determine key thermophysical properties—such as thermal conductivity and specific heat capacity—as well as electromagnetic characteristics, including dielectric loss factors. Initial moisture content and bulk density were also measured to provide a comprehensive profile of each sample prior to drying.

Drying experiments were conducted using a commercial microwave oven, with all trials carried out at the facilities of McGill University in Montreal, Quebec, Canada. This work was undertaken in close collaboration with Dr. Ferri Hassani's research group, and special acknowledgment is extended to Dr. Mehrdad Kermani and Dr. Adel Ahmadihosseini for their invaluable assistance in performing the experimental procedures.

## 2.1 Chapter Introduction

Four types of minerals were procured from a partner mining company, including Ammonium Sulphate (M1), Lasta Filter Residue (M2), Sparkler Cake (M3) and Zinc Pressure leach (M4) that are shown in **Figure 2.1(a) – (d)**, respectively. Due to presence of volatile elements such as sulphur, the toxic gas emission and burning are challenges in conventional kiln drying operations of these materials. Therefore, microwave heating is sought for as an alternative to achieve drying demands. For these materials, the thermophysical and electromagnetic properties were characterized as described in the next sections.



(a) Ammonium Sulphate (M1)



(b) Lasta Filter Residue (M2)



(c) Sparkler Cake (M3)



(d) Zinc Pressure leach (M4)

**Figure 2.1** Samples procured from a partner mining company.

## 2.2 Characterization of Material Properties

### 2.2.1 Initial Moisture Content

Shortly after receiving samples (and before all drying experiments), the initial moisture content of samples was measured. Samples weighing 275 g were placed inside a hot-air blown oven and remained overnight (24 hours) at 75 °C (**Figure 2.2**). Samples were weighed the next day and the

mass loss was used to calculate the initial (wet basis) moisture content ( $\varphi_0$ ) defined as  $\varphi_0 = \frac{W_0 - W_f}{W_0}$

where  $W_0$  and  $W_f$  are the sample weight before and after overnight drying, respectively. For each material, this procedure was repeated three times and the results are summarized in **Table 2.1**.



(a) Hot-air blown oven



(b) Overnight dried sample (M2)

**Figure 2.2:** (a) The hot-air blown oven used to measure initial moisture content, and (b) sample (M2) after 24hrs of drying.

**Table 2.1** Measured initial moisture content of as-received samples using overnight hot-air drying.

Material	Averaged Initial Moisture Content ( $R_1$ to $R_3$ are repeats)
M1	5.47% ( $R_1=5.39\%$ , $R_2=5.32\%$ , $R_3=5.71\%$ )
M2	26.32% ( $R_1=26.23\%$ , $R_2=26.35\%$ , $R_3=26.38\%$ )
M3	4.13% ( $R_1=4.21\%$ , $R_2=3.87\%$ , $R_3=4.31\%$ )
M4	13.40% ( $R_1=13.51\%$ , $R_2=13.49\%$ , $R_3=13.19\%$ )

## 2.2.2 Density

The collected samples were carefully placed into a measuring container that had clearly marked milliliter (mL) graduations. Both the initial mass and the height of the material inside the container were documented. Using the recorded weight and the measured volume, the density of each specimen was calculated. Compaction of the sample was avoided as much as possible to preserve its “as-received / as-is” condition. The obtained values are summarized and presented in **Table 2.2.**

**Table 2.2** Measured density of samples.

Material	Density ( $\text{g}/\text{cm}^3$ ) – as-received
M1	1.191
M2	1.964
M3	1.532
M4	1.690

### 2.2.3 Thermal Conductivity

Thermal conductivity measurements were carried out on both the untreated (as-received) and oven-dried specimens using the transient line heat source (TLH) technique [75], implemented through the KD2 Pro instrument. Compaction of the sample was avoided as much as possible to preserve its “as-received / as-is” condition. In this method, a slender probe is carefully inserted into the sample, where it functions both as a heating element and a temperature sensor (or, in some cases, in conjunction with a separate sensor). The probe introduces heat into the material over a set duration while simultaneously recording the temperature response. Data collection continues during the subsequent cooling phase to ensure accuracy. The resulting temperature–time profiles were processed to determine the thermal conductivity values of the samples, and these results are compiled in **Table 2.3**.

**Table 2.3** Measured thermal conductivity of as-received and fully dried samples.

Material	Thermal conductivity (W/m.K)	
	untreated (as-received) specimens	oven-dried specimens
M1	0.245	0.213
M2	0.663	0.274
M3	0.255	0.228
M4	0.479	0.213

## 2.2.4 Heat Capacity

The determination of heat capacity was conducted exclusively on the fully dried specimens using the differential scanning calorimetry (DSC) technique [76], with the temperature program extended up to 125 °C. Compaction of the sample was avoided as much as possible to preserve its “as-received / as-is” condition. In this analytical method, the sample is subjected to a controlled and constant heat flux, while its thermal response is continuously monitored. The recorded data allow for the quantification of the material’s heat capacity. For this study, a DSC Discovery 2500 instrument was employed to carry out the measurements. The obtained results are illustrated in **Figure 2.3.**

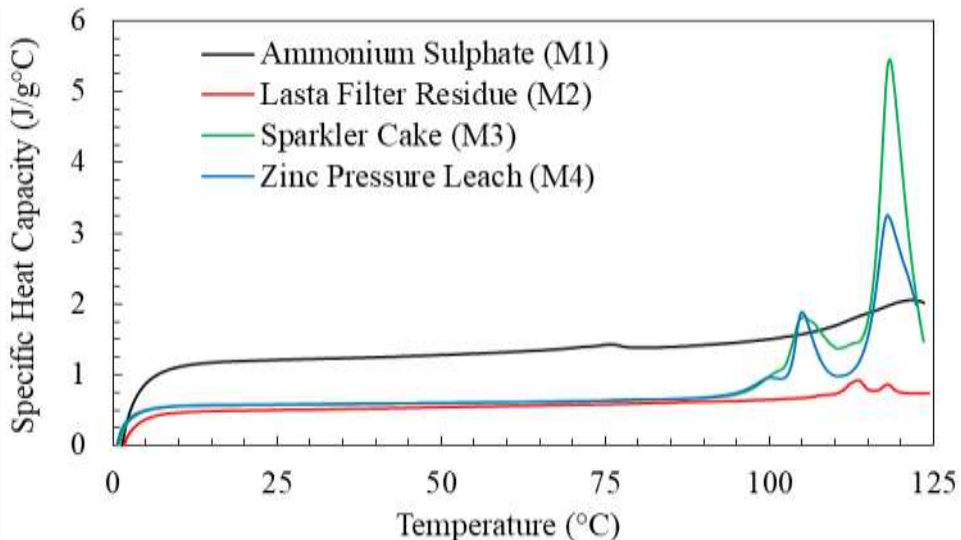
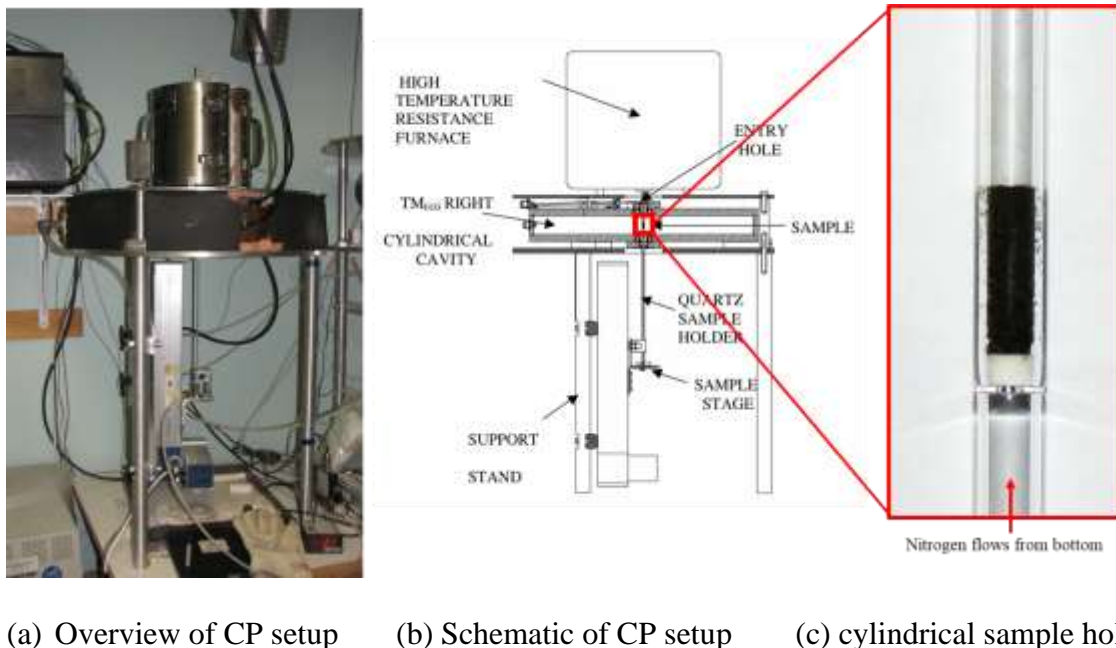


**Figure 2.3** Heat capacity measurements for four type of minerals.

## 2.2.5 Electromagnetic Properties

The dielectric characteristics of the materials were evaluated using the cavity perturbation (CP) method [77, 78]. A schematic representation of the experimental setup is provided in **Figure 2.4**, which illustrates the main components: the furnace, the resonant cavity, and the sample holder. In this approach, the sample is repeatedly introduced into and withdrawn from the cavity, and the corresponding frequency shifts are recorded to determine the dielectric response.



(a) Overview of CP setup      (b) Schematic of CP setup      (c) cylindrical sample holder

**Figure 2.4** Cavity perturbation setup (a) together with (b) schematic of parts and (c) a close look at sample holder.

The measurements were initiated at ambient conditions and continued with a stepwise increase in temperature of 20 °C until reaching 120 °C. Once the maximum temperature was attained, the samples were maintained at 120 °C for a duration of two hours, during which measurements were performed every 15 minutes. Subsequently, the specimens were cooled back to room temperature in reverse increments of 20 °C. To ensure accuracy in weight and density determinations, the

sample holder was carefully removed after each step while maintaining the sample's position and stability throughout the entire experimental sequence.

**Figure 2.5 to Figure 2.8** illustrate the dielectric response of the samples, represented in terms of the loss tangent ( $\varepsilon''/\varepsilon'$ ), as a function of their moisture content and temperature – with  $\varepsilon''$  and  $\varepsilon'$  being the imaginary and real parts of dielectric constant, respectively. The results clearly show that fully dried specimens demonstrate very limited interaction with the applied electromagnetic field. In contrast, samples containing water exhibit significantly stronger dielectric activity. This distinction indicates that microwave energy is primarily absorbed by the moisture fraction of the material, leading to preferential heating of the moisture. Such selective absorption not only enhances the effectiveness of microwave-assisted drying but also reduces unnecessary thermal exposure of the surrounding solid matrix, thereby improving overall energy efficiency and process control.

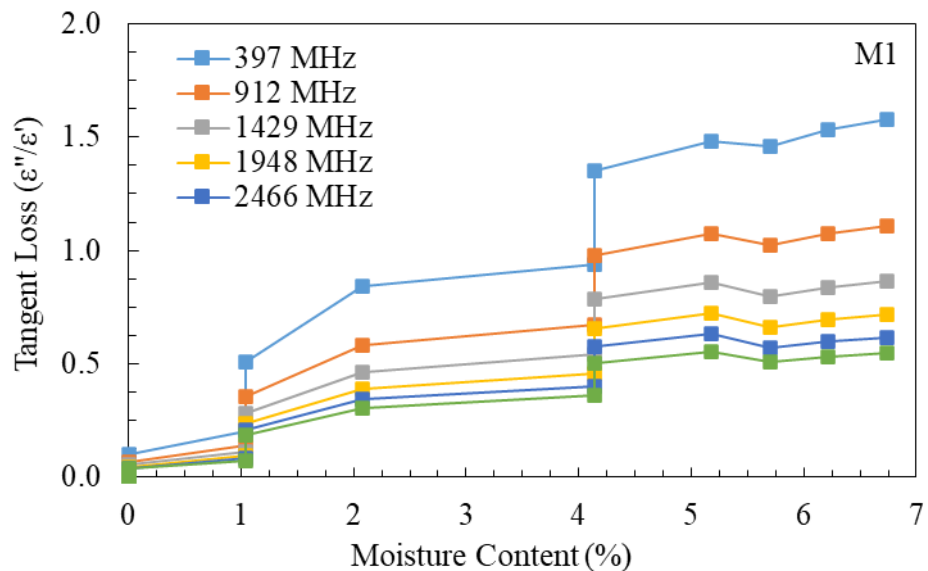


**Figure 2.5** Measured tangent loss of M1 at 5 different frequencies using cavity perturbation technique.

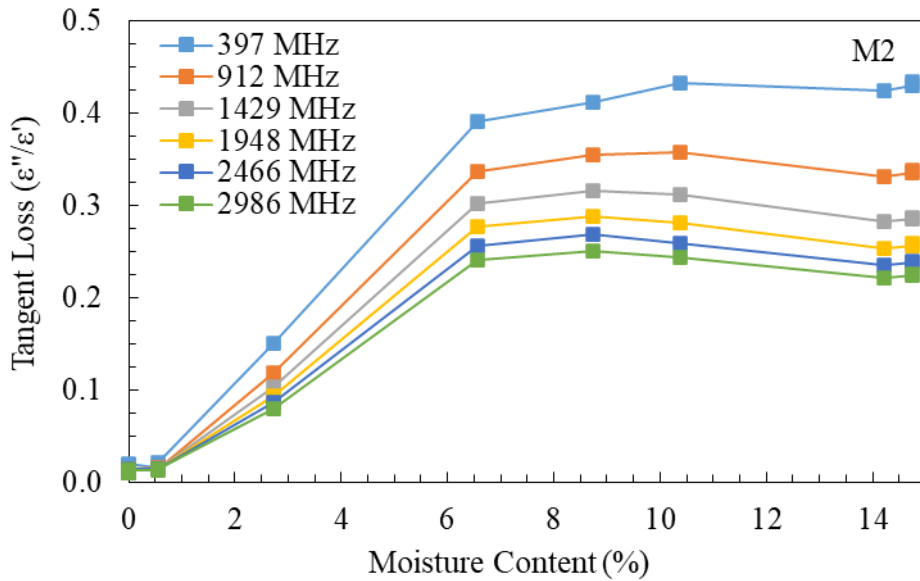


**Figure 2.6** Measured tangent loss of M2 at 5 different frequencies using cavity perturbation technique.

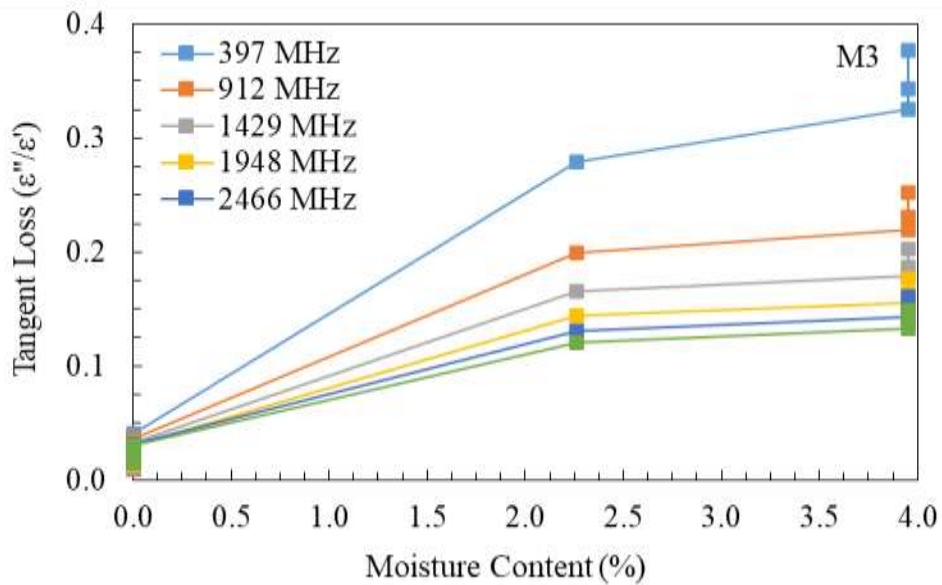


**Figure 2.7** Measured tangent loss of M3 at 5 different frequencies using cavity perturbation technique.

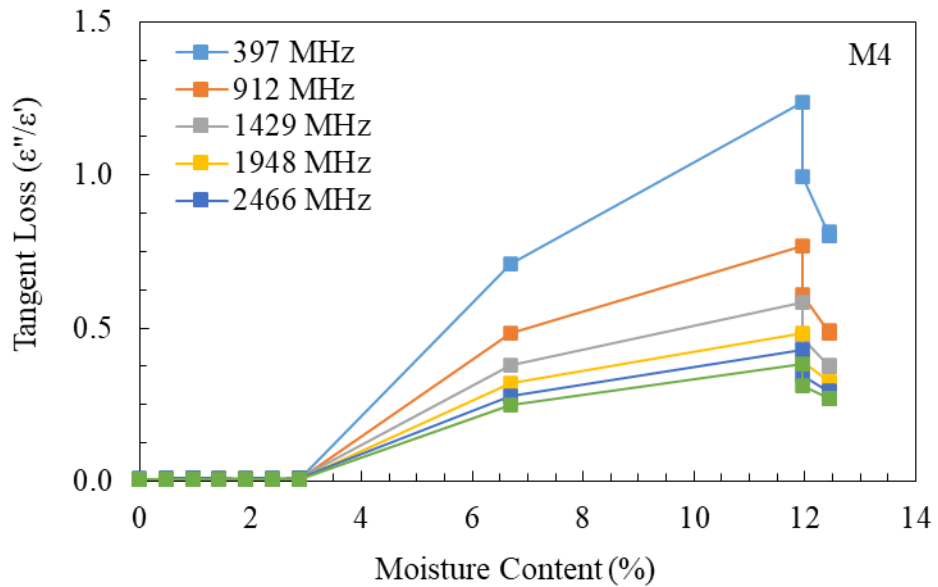


**Figure 2.8** Measured tangent loss of M4 at 5 different frequencies using cavity perturbation technique.

Previous studies [79] have reported that particulate systems—such as solids, fine powders, or granular composites containing inclusions, similar to materials studied in this work (see: **Figure 2.1**)—tend to exhibit a linear correlation between the density–normalized dielectric loss ( $\epsilon''/\rho$ ) and the density–normalized dielectric constant ( $\epsilon'/\rho$ ), with  $\rho$  being the density of the material. This relationship can be expressed mathematically as  $\epsilon''/\rho = \alpha(\epsilon'/\rho - \beta)$ , where  $\beta$  is a material-specific fitting parameter that only depends on the density, and  $\alpha$  is a frequency-dependent fitting coefficient, unique to each frequency. To evaluate this relationship for the current study, **Figure 2.9**, together with **Table 2.4**, present a plot of  $\epsilon''/\rho$  versus  $\epsilon'/\rho$  at an operating frequency of 2.45 GHz, considering all four categories of materials examined. This linear relationship can serve two key purposes: first, it provides a means to verify the reliability and consistency of the experimental measurements by leveraging a known characteristic of the material under investigation i.e.

granular; second, it can be applied for interpolation within the measurement range, thereby enabling more accurate estimation of dielectric properties at intermediate points where direct measurements may not have been taken.

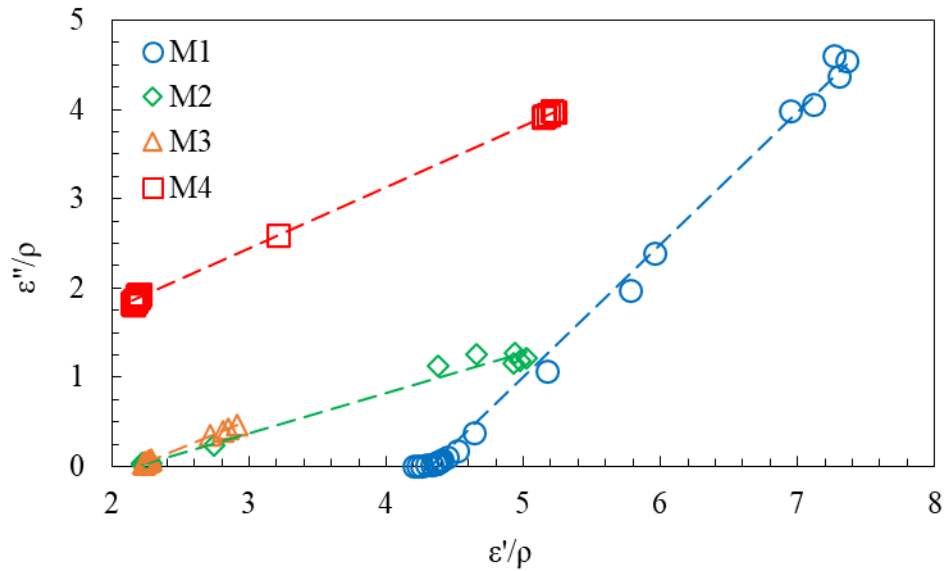


**Figure 2.9** The linearity relationship between  $\epsilon''/\rho$  and  $\epsilon'/\rho$  for the samples at a frequency of 2.45 GHz.

**Table 2.4** Fitting parameters evaluated for the linearity relationship for the samples at a frequency of 2.45 GHz.

Material	Slope ( $\alpha$ )	Intercept ( $\alpha \times \beta$ )	$\beta$
M1	1.49	-6.45	4.33
M2	0.45	-0.98	2.17
M3	0.64	-1.40	2.18
M4	0.69	0.38	-0.55

## 2.3 Microwave Drying Experiments

### 2.3.1 Overall Setup

Microwave heating experiments were conducted using a 3-kW microwave oven (manufacturer-rated forward power) operating at a frequency of 2.45 GHz, as illustrated in **Figure 2.10**. The mass of the samples during testing was monitored with a benchtop analytical balance capable of a precision of  $\pm 10$  mg, ensuring accurate weight tracking. In addition, surface temperature distributions were captured using an infrared (IR) thermal imaging camera, which provided spatially resolved information on heating behavior across the sample surface.



**Figure 2.10** Experimental setup showing a 3kW microwave oven, benchtop scale and an IR thermal camera.

### 2.3.2 Microwave Ramp-up Time and Effective Forward Power

To assess both the ramp-up period and the actual forward power delivered, a thermal energy absorption test [80] was performed using 150 g of water exposed to microwave irradiation in increments of up to 15 seconds. For each heating interval, the increase in temperature and the corresponding mass change were recorded, enabling calculation of the net energy absorbed by the water. The results, summarized in **Figure 2.11**, indicate a ramp-up time of approximately 2.94 seconds, obtained by solving the equation  $1539 \times t - 4527.6 = 0$ . Furthermore, the slope of the linear temperature–time relationship yielded an effective forward power of about 1539.1 W. These findings demonstrate that, although the microwave system is nominally rated at 3 kW, a fraction of the input energy is dissipated within the waveguide and associated components before reaching the cavity, resulting in a lower absorbed power by the sample.

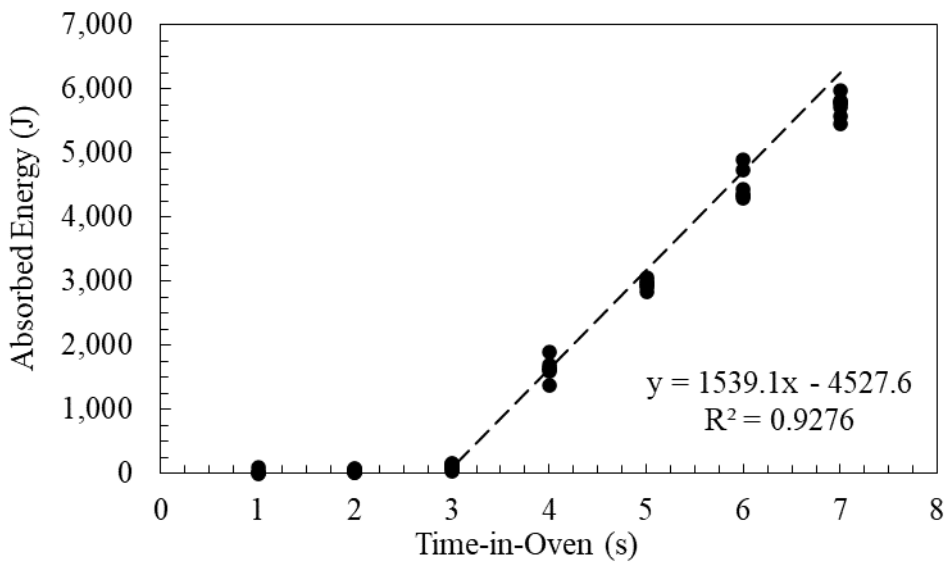


**Figure 2.11** Measured load energy absorption for ramp-up time of the microwave oven.

### 2.3.3 Microwave Drying Tests

Samples, each with a mass of 275 g, were filled into Pyrex glasses where compaction of the sample was avoided as much as possible to preserve its “as-received / as-is” condition. Samples were placed inside the microwave system and subjected to controlled, incremental microwave energy exposures at two initial dosage levels: 15 kWh/t and 30 kWh/t. Irradiation continued until the moisture content of the samples was reduced to below 1%. During the process, samples were allowed to cool whenever the surface temperature approached approximately 100 °C to prevent overheating. Mass changes were recorded using a benchtop analytical balance with a precision of  $\pm 0.001$  g, ensuring accurate monitoring of moisture loss. Surface temperature measurements were performed using an infrared thermometer (Etekcity Lasergrip 1022D). The combined data from temperature and mass variation were then used to calculate the total thermal energy absorbed by each sample throughout the drying process.

In **Figure 2.12** to **Figure 2.15**, the maximum surface temperature of the materials is plotted against their moisture content are illustrated. Initially, the samples exhibit a temperature increase without significant mass loss, suggesting that the microwave energy is primarily used to raise the temperature of the material. This phase is followed by a plateau in temperature accompanied by a steady reduction in moisture content, indicating active drying. As the moisture content falls below approximately 1%, the surface temperature begins to rise again, while the rate of moisture loss diminishes. This behavior reflects a limitation in the internal mass transfer of evaporated water; the trapped moisture inside the material allows for additional conductive heat exchange with the solid matrix, resulting in the observed temperature increase.

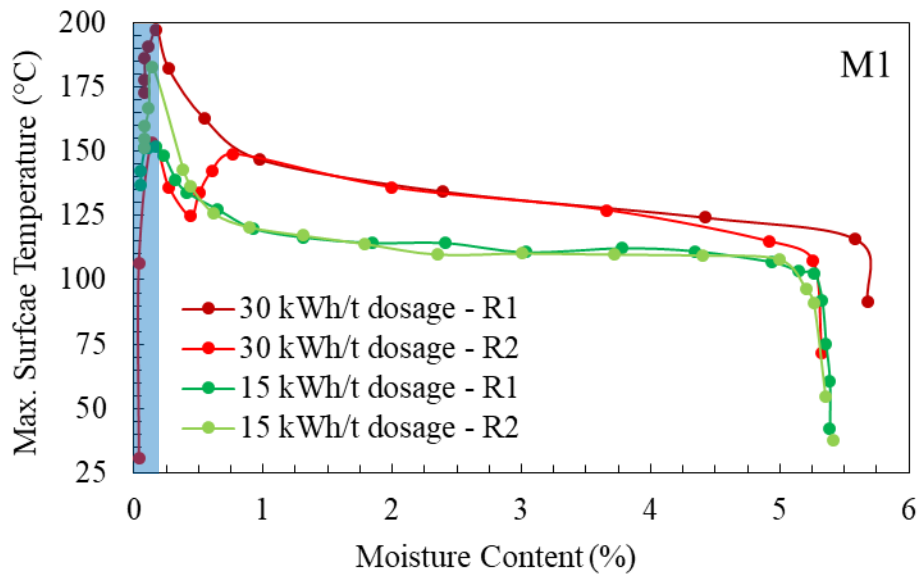


**Figure 2.12** Measured changes in maximum surface temperature for M1 (shaded area shows the datapoints collected during cooling – outside microwave cavity).

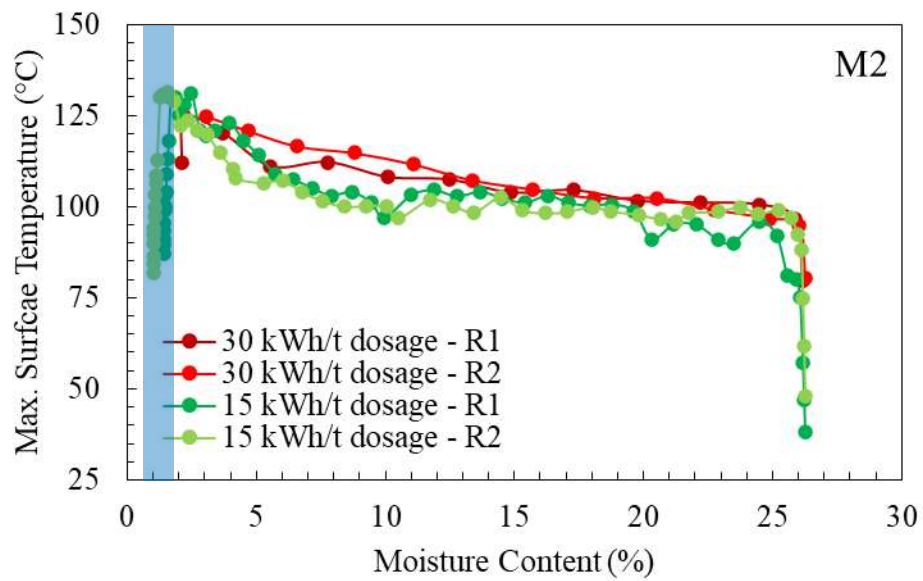


**Figure 2.13** Measured changes in maximum surface temperature for M2 (shaded area shows the datapoints collected during cooling – outside microwave cavity).

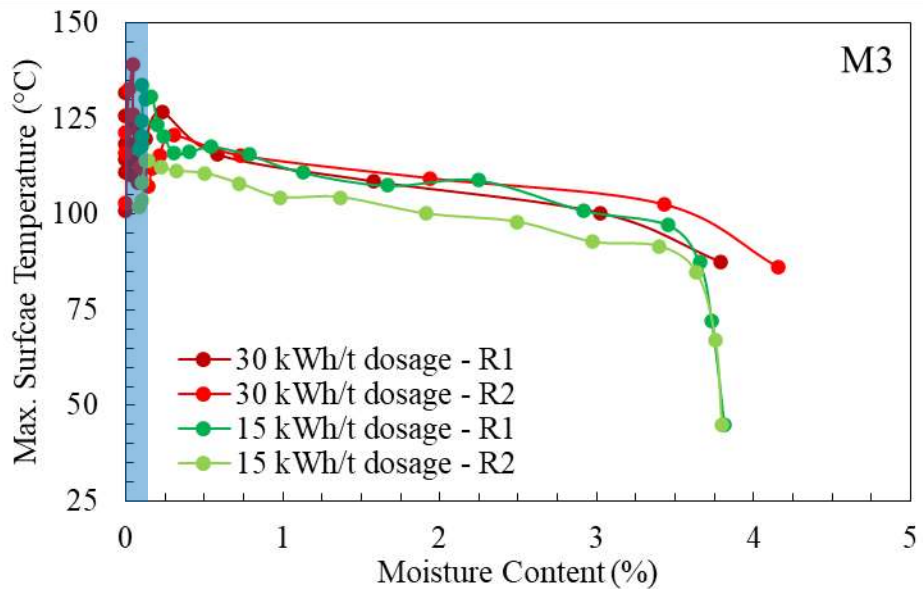


**Figure 2.14** Measured changes in maximum surface temperature for M3 (shaded area shows the datapoints collected during cooling – outside microwave cavity).

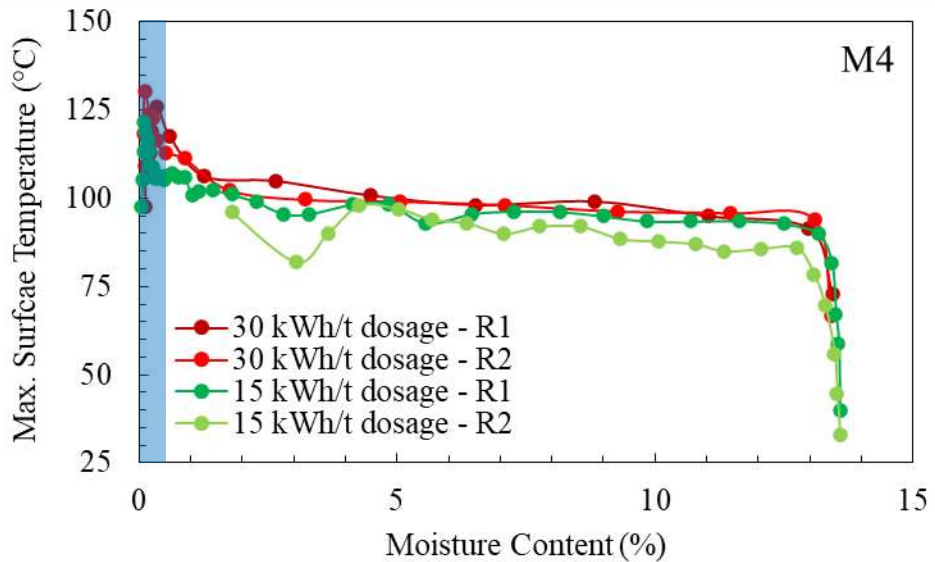


**Figure 2.15** Measured changes in maximum surface temperature for M4 (shaded area shows the datapoints collected during cooling – outside microwave cavity).

In **Figure 2.16** to **Figure 2.19**, the relationship between moisture loss and the cumulative microwave energy absorbed by the material are shown. Initially, as energy is delivered, the rate of moisture loss is minimal, corresponding to the preheating stage. Once the moisture reaches its evaporation temperature, it begins to evaporate at a nearly constant rate, indicating that microwave energy is preferentially absorbed by the water content within the material.

When comparing low-dose and high-dose energy profiles, it is evident that lower microwave dosages allow for more precise control of temperature fluctuations, producing more uniform thermal profiles across the material. This suggests that, in a continuous processing scenario, employing low-dose compartments or repeated low-energy stages could be an effective strategy to achieve the desired moisture content while maintaining better thermal regulation. Such an approach could optimize drying efficiency while minimizing overheating and potential thermal degradation of the materials.

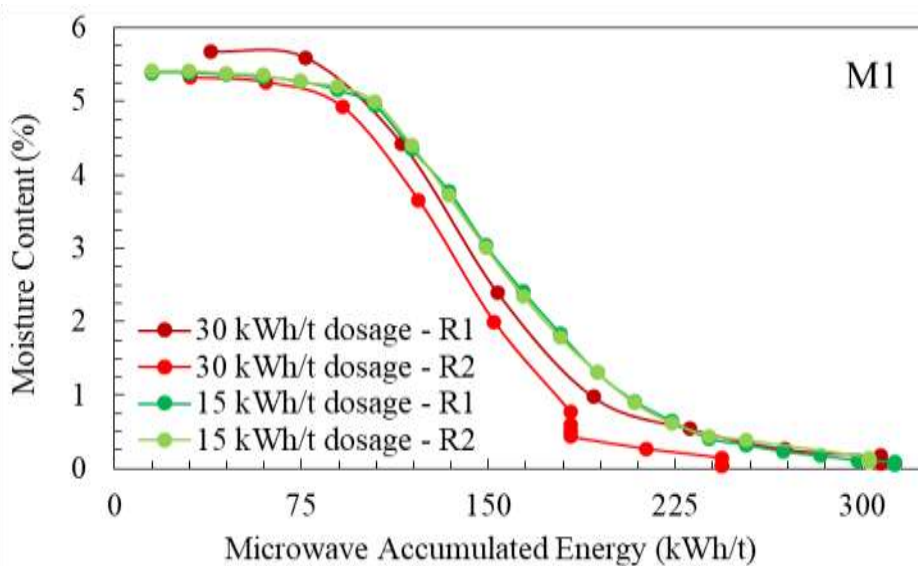


**Figure 2.16** Measured changes in mass for M1.

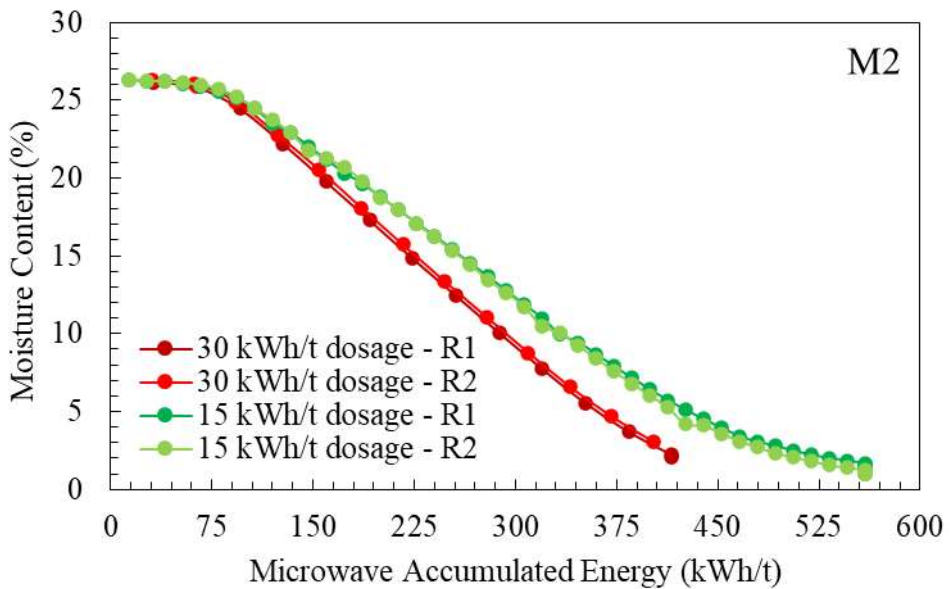


**Figure 2.17** Measured changes in mass for M2.

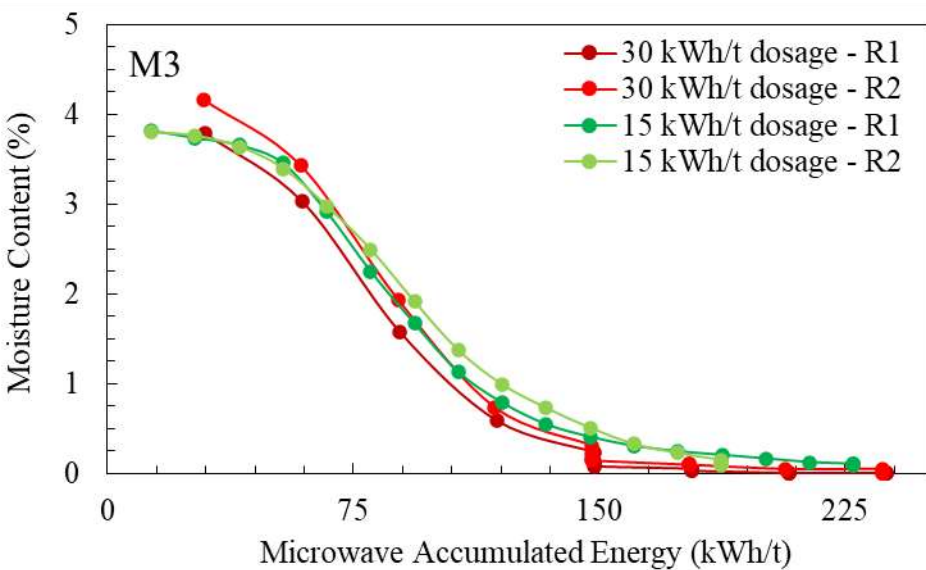


**Figure 2.18** Measured changes in mass for M3.

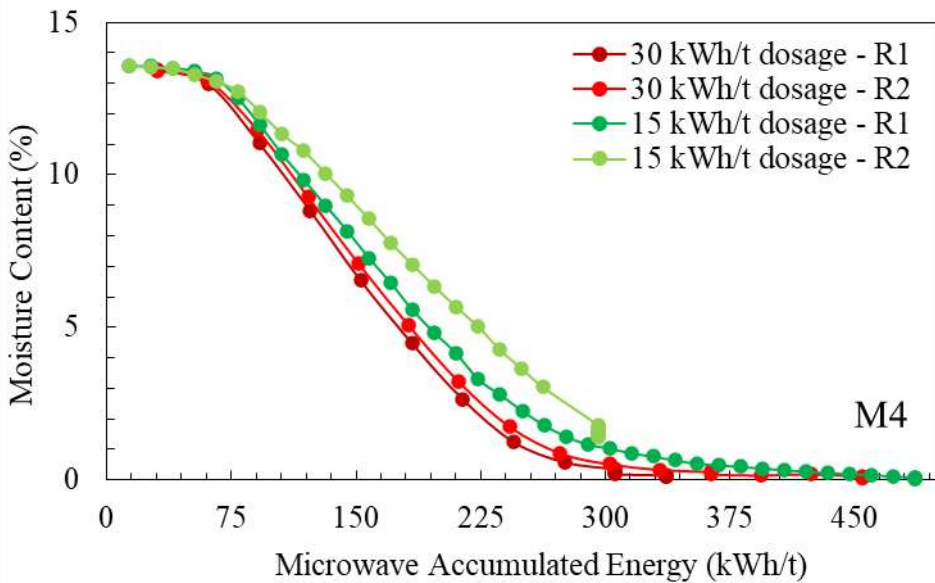


**Figure 2.19** Measured changes in mass for M4.

**Table 2.5** summarizes the residual moisture content of the tested materials after microwave treatment, alongside the intended target moisture levels. The data reveal that higher microwave energy inputs do not result in a substantially greater reduction in moisture compared to lower energy doses. Instead, the primary distinction between the treatments lies in the degree of temperature control during the drying process. Applying lower microwave energy over an extended period enables more precise regulation of temperature changes, thereby reducing the likelihood of localized overheating and promoting a more uniform drying profile throughout the sample. These findings suggest that, in scenarios where both thorough moisture removal and preservation of thermal stability are essential, a prolonged low-dose microwave approach is the most effective strategy. Such a method optimizes the balance between drying efficiency and the integrity of the material's properties.

**Table 2.5** Effect of microwave energy dosages on moisture loss.

	M1	M2	M3	M4
Initial Moisture Content (%) – As-received	5.47	26.32	4.13	13.4
Target Moisture Content (%)	0.2-0.6	1	<1	<1
Final Moisture Content (%) – 15 kWh/t	0.07	1.15	0.08	0.73
Final Moisture Content (%) – 30 kWh/t	0.015	0.23	0	0.09

## 2.4 Chapter Conclusion

The results of these experiments demonstrate that microwave heating represents a promising and effective method for drying mineral materials. This approach can potentially achieve complete moisture removal because microwave energy is absorbed selectively by water rather than by the mineral matrix. This selectivity arises from the substantial difference in dielectric loss factors between water and the minerals' constituent elements, allowing efficient and targeted heating of moisture without excessive heating of the solid phase.

To develop a deeper understanding of the drying process and to examine internal temperature variations—parameters that are difficult to access experimentally and often limited in accuracy when using localized sensors such as thermocouples—a numerical model has been formulated. The model, presented in the next chapter, is designed to simulate the internal thermal and moisture dynamics within the material during microwave drying. It will be validated using experimental data specifically collected for material M2, thereby ensuring the reliability of the model for predicting and optimizing microwave-assisted drying processes.

## **Chapter 3: Numerical Model Development and Experimental Validation**

In this chapter, material M2 was selected as the representative sample for the development of a numerical model of microwave heating. To ensure accuracy and improve the reliability of the dataset, a series of single-shot experiments were performed. This approach minimized the measurement uncertainties that often arise in continuous drying tests, where samples are repeatedly removed and reinserted into the microwave oven.

The modeling framework was established by deriving the governing physical equations, implementing them within COMSOL Multiphysics, and defining the corresponding solution strategies. To support the simulations with realistic material properties, additional characterization of M2 was carried out, including the determination of porosity, solid density, and thermal conductivity. These experimentally obtained parameters served as critical inputs for achieving a robust and accurate numerical representation.

The following sections of this chapter provide a comprehensive account of the experimental investigations, the theoretical formulation, and the step-by-step development of the numerical model, as well as its validation against measured data.

A version of this chapter has been **submitted** as a research article:

- Milad Asgarpour Khansary, Parham Samea, and Seyed Ali Ghoreishi-Madiseh. (2025) Microwave Drying of Minerals with Moisture-Dependent Properties: Experimental and Numerical Analysis.

### **3.1 Chapter Introduction**

The material M2 examined in this chapter consists of feedstocks used in the smelting process, representing their state prior to drying and subsequent injection into smelting shafts. Specifically, this material—Lasta Filter Residue—exits the mechanical press at approximately 50 °C with a moisture content near 25%. It is then fed into a conventional kiln dryer with the objective of reducing its moisture content to around 15% at the outlet. Due to its sulfur content, the industrial partner has reported incidents of flames and sulfur combustion, prompting the recommendation of a maximum operational temperature of 120 °C to ensure safety. Beyond the risk of sulfur emissions, additional challenges include uneven drying and the tendency of the material to adhere to and accumulate on dryer walls, which can compromise product quality. M2 was therefore selected to assess the performance and feasibility of microwave heating as an alternative drying method, including its potential application as a retrofit option for existing drying systems.

The moisture content of M2 was found to be variable, and changes were anticipated during transport to the University of British Columbia and subsequent storage. To account for this variability, additional characterizations were carried out, including measurement of moisture content prior to each drying test, as well as evaluations of density and porosity.

The microwave drying experiments were designed to reduce experimental errors. Each sample was exposed to microwave irradiation only once, followed immediately by measurements of mass loss and surface temperature. Before conducting the drying tests, the microwave oven available at the Coal and Minerals Processing Laboratory of the University of British Columbia was characterized for key operational parameters, including ramp-up time, forward power, air inflow from fans, and rotation of the stirrers. These empirical observations were compared against predictions from a numerical model developed in this study.

In constructing the numerical model, particular attention was given to the accurate integration of moisture- and temperature-dependent material properties. Previous models that incorporated complex transport equations without accounting for these dependencies often failed to achieve reliable predictive accuracy. The model developed here couples the electromagnetic and thermal fields within COMSOL Multiphysics, using the experimentally characterized moisture-dependent properties. The electric field is solved first, and the resulting resistive power loss is applied as a heat source in the temperature field. This two-step calculation is repeated at intervals of 0.4375 seconds until the target irradiation time for each experiment is reached.

The subsequent sections provide a detailed description of both the experimental characterization performed on material M2 and the numerical modeling methodology developed in this work.

## 3.2 Experimental Section

### 3.2.1 Detailed Characterization of Material M2

#### 3.2.1.1 Initial Moisture Content

The starting moisture level of the samples was assessed by subjecting them to oven drying at a controlled temperature of 75 °C for a continuous period of 24 hours. After drying, the moisture content was estimated using the expression  $M_i = 100 \times \frac{W_i - W_f}{W_i}$ , where  $W_i$  corresponds to the original mass of the sample prior to drying, and  $W_f$  represents the mass measured after the drying process. The calculated values for each trial are presented in **Table 3.1**. Based on these measurements, the mean initial moisture content of the materials was obtained as 20.1%. The data exhibited a high level of precision, with a relative standard deviation of only 0.25%, confirming the reliability of the results.

**Table 3.1** Initial moisture measurement of material M2.

Sample (#)	Initial weight (g)	Final weight (g)
1	275.00	218.20
2	275.00	218.17
3	275.20	218.61
4	275.21	218.65
5	275.14	219.09
6	275.10	218.41

### 3.2.1.2 Density

The bulk wet and dry densities were measured by placing wet and dry samples carefully into a measuring container that had clearly marked milliliter (mL) graduations. Both the initial mass and the height of the material inside the container were documented. Using the recorded weight and the measured volume, the density of each specimen was calculated. Compaction of the sample was avoided as much as possible to preserve its “as-received / as-is” condition. The density of the solid was determined using the principle of Archimedes, in which the displacement of water served as the basis for volume estimation. For accuracy, the immersion medium was considered to be pure water, free from impurities or dissolved constituents that might otherwise influence the results [81, 82]. To isolate the characteristics of the solid phase, the oven-dried materials were ground into fine powders, thereby minimizing the influence of trapped air pockets or residual porosity.

Experimental observations, illustrated in **Figure 3.1**, provided density values for three different states of the material. The density of the oven-dried specimens was calculated as  $\rho_d = 1433.6 \text{ kg/m}^3$ . In comparison, the density of the moist/wet samples, representing the condition of the material at its initial moisture content ( $M = M_i$ ) was found to be  $\rho_m = 1803.5 \text{ kg/m}^3$ . For the solid, pore-free phase, the density reached a significantly higher value of  $\rho_s = 2698.1 \text{ kg/m}^3$ . These results highlight the clear distinctions in material behavior between the dry, moist, and solid states.

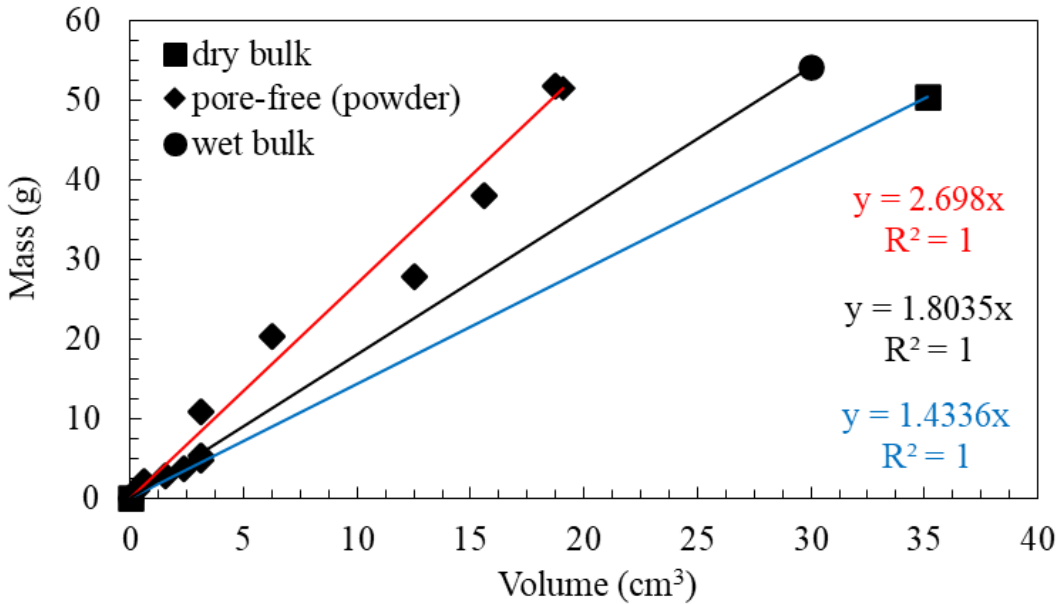


**Figure 3.1** Measured densities of wet, dry and solid (pore-free) material M2.

### 3.2.1.3 Porosity

The porosity of the material was evaluated by employing bulk density data in conjunction with the expression  $\varphi = 1 - \rho_d / \rho_s$  [83]. Using this approach, the calculated porosity of the investigated samples was approximately  $\varphi = 46.86\%$ . It is important to emphasize that this estimation is based solely on the relationship between dry bulk density and solid-phase density. Variations in moisture levels, which can influence the distribution of void spaces and thereby alter porosity values [84], were not incorporated into the scope of the present analysis.

### 3.2.1.4 Thermal Conductivity

Following recommendations from several studies [85-87], the geometric mean model was selected in this work as a reliable approach for estimating the effective thermal conductivity of mineral-based materials. The general form of the model is expressed as  $k = \prod k_i^{x_i}$ , where  $k_i$  and  $x_i$  are

the thermal conductivity and volume fraction of phase  $i$ . Thermal conductivity measurements were performed using the KD2-Pro Thermal Properties Analyzer, which provides results with an accuracy of approximately  $\pm 10\%$ . This uncertainty range was explicitly considered when calculating the thermal conductivity of the studied material across varying moisture contents (**Figure 3.2**). Accounting for this factor is essential, as even moderate deviations in thermal conductivity can significantly influence the accuracy of evaporation simulations and related numerical predictions [88]. To determine the thermal conductivity of the solid phase, the dry condition was approximated as a two-phase system composed of solid material and air, where the conductivity of air was taken as  $k_{\text{air}} = 0.025 \text{ W/m.K}$ . Based on this assumption, the nominal conductivity of the solid phase was calculated to be  $k_s = 1.79 \text{ W/m.K}$ . Considering the instrument's  $\pm 10\%$  error margin, the corresponding conductivity limits were estimated as  $k_{s,\text{min}} = 1.51 \text{ W/m.K}$  at a  $+10\%$  error margin and  $k_{s,\text{max}} = 2.16 \text{ W/m.K}$  at a  $-10\%$  error margin.

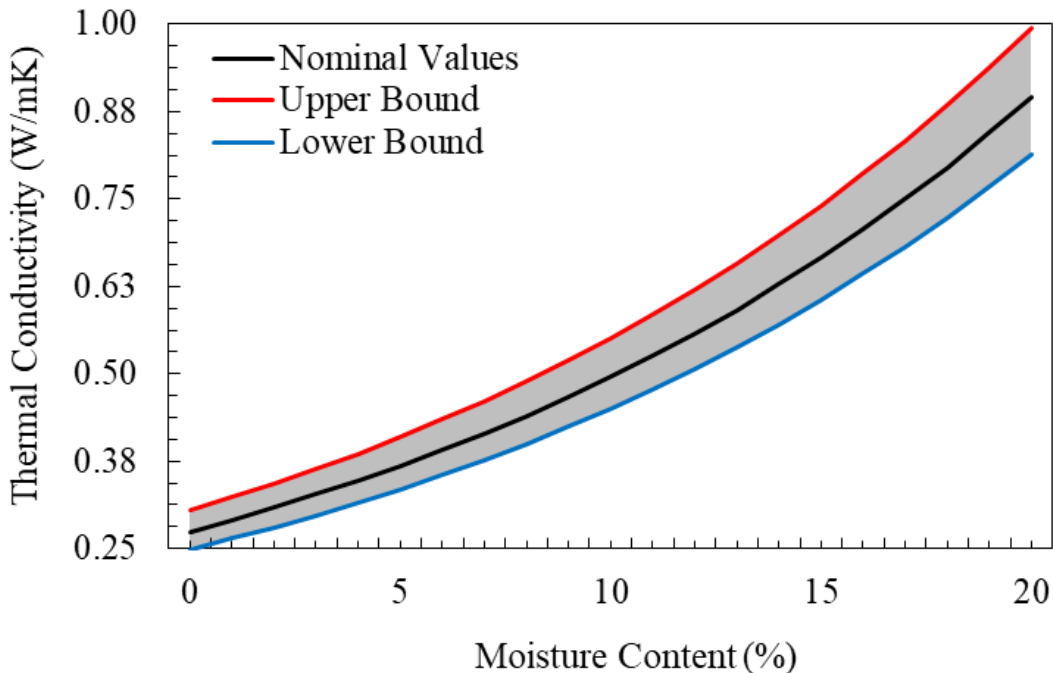


**Figure 3.2** Nominal thermal conductivity of the material determined using the geometric mean model.

Despite the established guidelines [85-88], many reports in the field have relied on the default thermal conductivity models provided by simulation software, with the arithmetic mean model being one of the most commonly employed approaches. To underscore the significance of choosing an appropriate mixture model, the present study examines the performance of the arithmetic mean model, defined as  $k = \sum x_i k_i$ . The thermal conductivity of the solid phase in the arithmetic mean model can be calculated as  $k_s = 0.47 \text{ W/m.K}$ , with respective  $k_{s,\min} = 0.43 \text{ W/m.K}$  at a +10% error margin and  $k_{s,\max} = 0.53 \text{ W/m.K}$  at a -10% error margin. These values are markedly lower than those computed when employing the recommended thermal conductivity model i.e. the geometric mean model.

### 3.2.2 Microwave Drying Tests

#### 3.2.2.1 Overall Setup

**Figure 3.3** illustrates the experimental arrangement employed for the drying tests. The system was composed of several key components: (1) a microwave oven rated at 3 kW with an operating frequency of 2.45 GHz, served as the primary heating source; (2) a precision bench scale capable of detecting mass variations as small as 10 mg, used for continuous monitoring of sample weight during drying; (3) an infrared (IR) thermal imaging camera to capture surface temperature distribution of the material; (4) a power analyzer designed to measure and record the electrical energy consumption of the microwave unit; and (5) a digital camera that provided real-time visual documentation of both temperature evolution and mass change throughout the experiment.

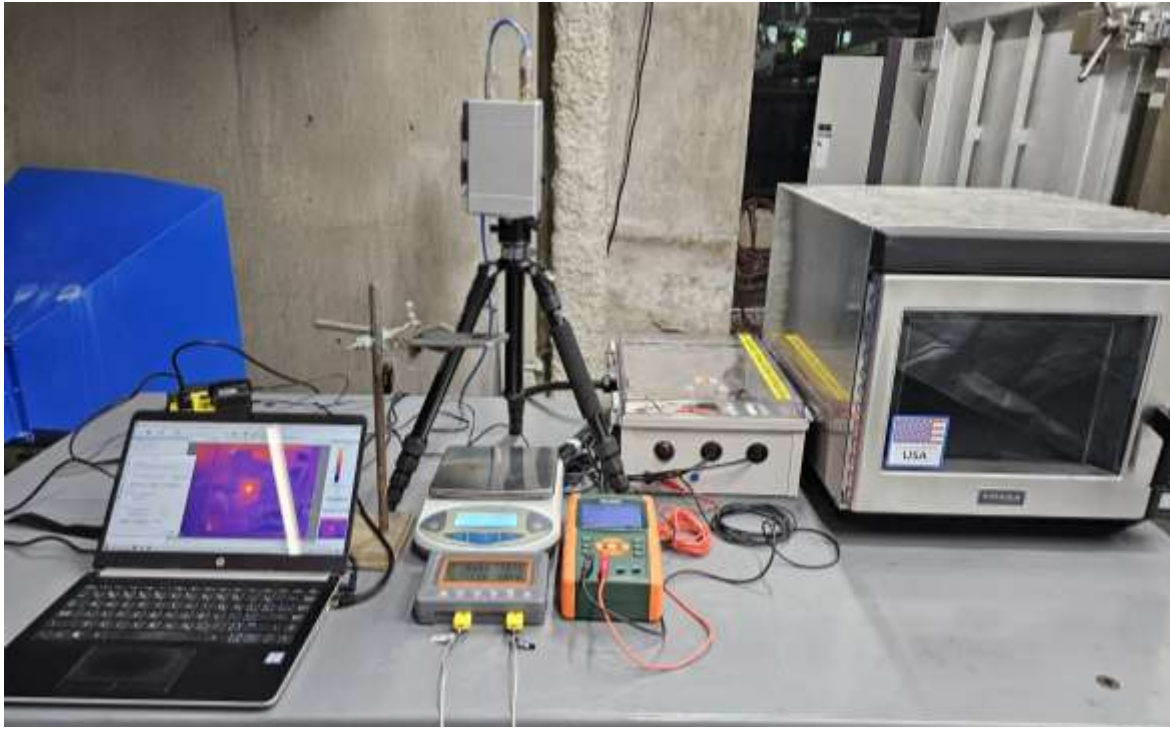


**Figure 3.3** Full experimental setup used to perform microwave drying tests.

### 3.2.2.2 The Microwave Oven

The microwave heating experiments were carried out using a 3-kW industrial microwave unit (Amana RC30S2) operating at the standard frequency of 2.45 GHz. The system was powered by three independent magnetron sources, each coupled to the cavity via rectangular waveguides configured in the TE<sub>10</sub> mode. To reduce the risk of localized overheating and thermal runaway, a ceramic plate was placed at the bottom of the cavity, ensuring more stable thermal performance during operation [89]. Once the microwave energy entered the cavity, its spatial distribution was regulated by three mechanical mode stirrers. These devices were incorporated to improve the uniformity of the electromagnetic field, which in turn reduced the likelihood of nonuniform drying that often results from irregular power deposition [90, 91]. The stirrers were installed with a 90° phase offset relative to each other and rotated steadily at an angular speed of 1.795 rad/s, thereby

promoting consistent field mixing and more homogeneous exposure of the samples to microwave energy.

### 3.2.2.3 Ramp-up Time

The ramp-up behavior of the magnetrons—defined as the period required to reach a steady and stable power output [92]—was investigated using two independent yet complementary measurement techniques. First, the electrical input power was monitored by connecting the microwave oven to an Extech 382100 Power Analyzer/Datalogger, which continuously recorded the power drawn from the grid. Second, the actual thermal energy absorbed by a test load of water was evaluated to provide a direct assessment of microwave energy transfer efficiency [93]. In the meantime, 140 g of tap water contained in a Pyrex glass vessel was placed inside the microwave cavity and exposed to irradiation for varying durations of 3, 4, 5, 6, 9, and 12 seconds. After each trial, both the temperature increase and the change in water mass were measured, allowing the absorbed energy to be determined. Meanwhile, the power analyzer logged input power at intervals of 2 seconds. Analysis of the power consumption data (**Figure 3.4**) indicated that the magnetrons required roughly 4 seconds to stabilize after activation. In contrast, the water load absorption experiments provided a slightly more refined estimate of the ramp-up period, calculated as approximately 3.07 seconds (**Figure 3.4**). Together, these two methods offered a comprehensive evaluation of the transient performance characteristics of the magnetrons.

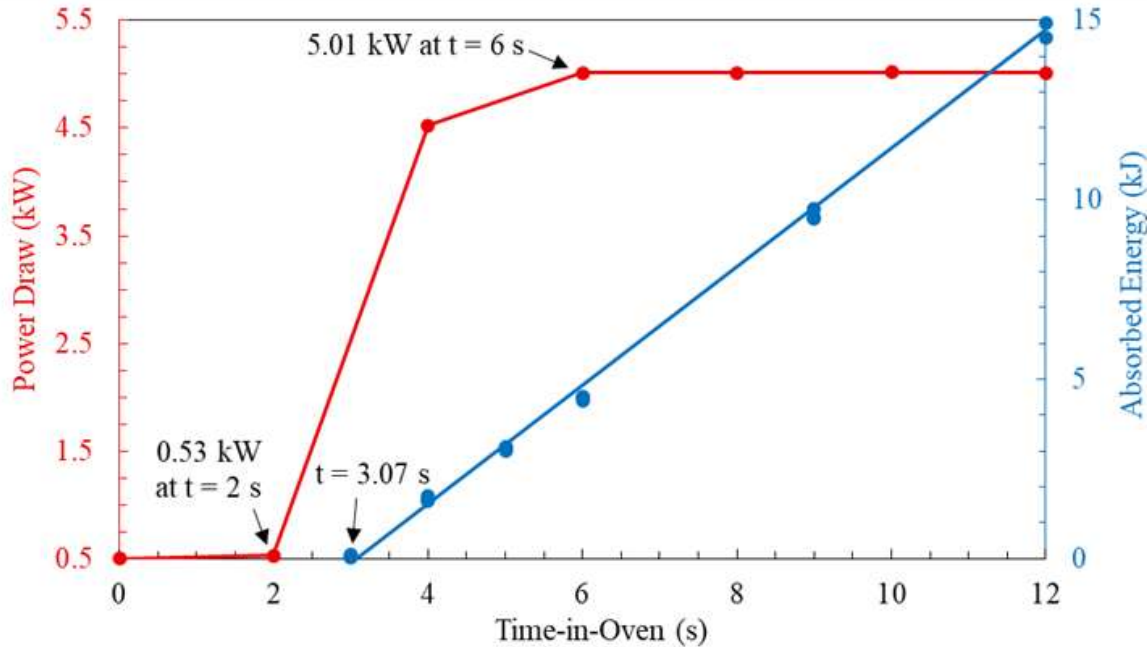


**Figure 3.4** Measured ramp-up time using thermal energy absorbed by 140 g of water at different exposure times.

### 3.2.2.4 Forward Power

The effective forward power output of the microwave oven was quantified in accordance with the IEC 60705:2010 + A1:2014 testing protocol [80]. To perform the assessment, tap water loads of varying masses—0.3, 0.5, 0.75, 1.0, 1.5, and 2.0 kg—were sequentially placed in the microwave cavity and irradiated for a fixed duration of 60 seconds. During each trial, the total amount of energy absorbed by the water was determined from measurements of both temperature increase and mass loss. Mass variations caused by evaporation were captured with a high-precision benchtop scale, while temperature changes were recorded using an Etekcity Lasergrip 1022D infrared thermometer. Simultaneously, the electrical power drawn from the grid was logged at 2-second intervals with an Extech 382100 Power Analyzer/Datalogger, ensuring an accurate record of the input energy profile. Based on these combined observations, the average forward power

delivered by the microwave system was determined to be approximately 2.55 kW, highlighting the actual usable microwave power for heating applications.

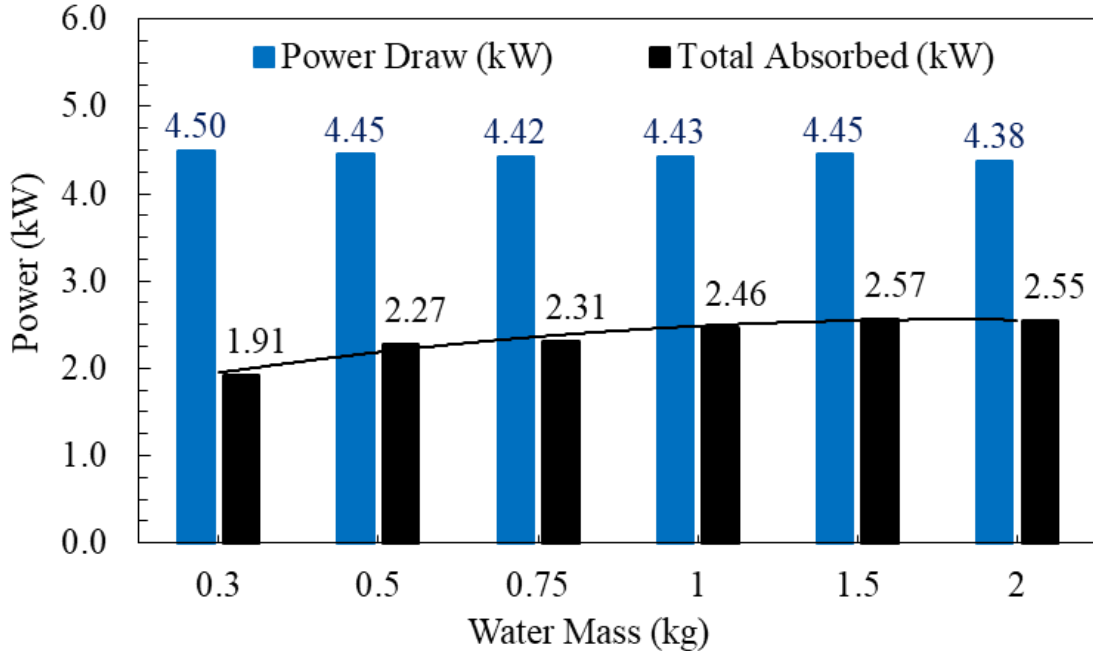


**Figure 3.5** Measured forward power.

### 3.2.2.5 Air inflow

To regulate the internal environment of the microwave cavity, an external air stream was introduced through two rectangular ducts, allowing continuous removal of water vapor and thereby reducing the possibility of moisture reabsorption or hygroscopic effects [94]. In addition to vapor extraction, the airflow served an important thermal role by promoting convective heat transfer between the exposed surfaces of the material and the surrounding air within the cavity [95]. The velocity of the incoming air was quantified using an anemometer, and the recorded values are summarized in **Table 3.2**. From these measurements, the mean inflow velocity was determined to be approximately 4.65 m/s. This experimentally obtained value was subsequently adopted in the

numerical heat transfer model, where it was implemented as a prescribed boundary condition representing forced convection at the sample–air interface.

**Table 3.2** Measured airflow into the cavity through two rectangular meshed entrances using an anemometer.

Case no.	Entrance no. 1		Entrance no. 2	
	State	Airflow (m/s)	State	Airflow (m/s)
1	Blocked		Open	6.9
2	Open	6.1	Blocked	
3	Open	4.5	Open	4.8

### 3.2.2.6 Single-shot Microwave Drying Tests

A series of single-run microwave drying tests were carried out on samples with an initial mass of 275 g, as detailed in **Table 3.3**. Each sample was carefully placed at the center of the microwave cavity atop the ceramic plate and subjected to microwave exposure for predetermined durations of 12, 15, 30, 45, and 60 seconds. Immediately following irradiation, the samples were removed, and their mass loss was measured using a high-precision benchtop balance with a resolution of  $\pm 0.01$  g. After mass measurements, the surface temperature distributions of the samples were captured using an infrared (IR) thermal imaging camera. During this process, the samples were briefly transferred from the oven to a location beneath the IR camera, where they were placed on a scale to maintain stability while the thermal images were recorded. The time elapsed during this transfer—from oven removal to image acquisition—is defined as the handling time and was documented for each measurement to ensure accurate interpretation of surface temperature data.

**Table 3.3** The details of microwave drying experiment.

Test	Time-in-Oven (s)	Energy Dosage (kW. hr/t)	Handling Time (s)
I	12	25.89	10
II	15	34.98	17
III	30	80.44	11
IV	45	125.89	11
V	60	171.35	16

### 3.3 Numerical Section

In microwave heating processes, the interaction between electromagnetic fields and heat transfer must be taken into account, as the two phenomena are inherently interdependent [96]. Mathematically, a local-in-time solution for this coupled system is always guaranteed to exist [97]. The subsequent distribution and dissipation of the generated heat are influenced by the material's thermal diffusivity, which represents the ratio of its heat capacity to thermal conductivity [98]. However, the material's thermal response to electromagnetic energy absorption is not instantaneous.

Due to this non-instantaneous response, it is not strictly necessary to solve the electromagnetic and heat transfer equations simultaneously as a single, tightly coupled system that encompasses all dependent variables in one matrix [99]. Instead, a more practical approach is to employ a loosely coupled, or sequential, solution scheme. In this framework, the electromagnetic field and temperature field are solved separately, but information is exchanged bidirectionally and iteratively between the two domains to ensure convergence and consistency [100]. The procedure for implementing this sequential coupling approach is described in detail below.

#### 3.3.1 Governing Equations

The electric field propagates through materials at an extremely high speed, nearly equivalent to the speed of light, while its magnitude and direction fluctuate on the order of nanoseconds, corresponding to the operating frequency of 2.45 GHz. Typically, this propagation exhibits a harmonic behavior and can be expressed as  $E(t) = E_0 e^{i\omega t}$ , where  $\omega$  is the angular frequency, related to the conventional frequency ( $f$ ) as  $\omega = 2\pi f$  [101]. Here,  $E_0$  is the amplitude of the electric field and  $t$  is the traveling time. The harmonic nature of the electric field suggests that the

time-dependent Maxwell's equations governing its behavior can be transformed into the frequency domain using a Fourier transform. This transformation significantly reduces computational complexity, making numerical simulations more efficient.

However, it should be noted that for materials with high permittivity values (both real and imaginary components  $\epsilon', \epsilon'' > 10$ ), solving the equations directly in the time domain is generally recommended. This approach helps prevent ill-conditioning in the resulting algebraic matrices and can lead to faster, more stable solutions [102]. In the case of microwave heating of minerals, where materials usually exhibit low permittivity ( $\epsilon', \epsilon'' < 10$ ), the frequency-domain solution approach is most commonly applied in the literature due to its computational advantages and suitability for low-permittivity media.

The spatial and temporal distribution of the electric field ( $E$ ) is governed by Maxwell's equations, which, for the considered scenario, can be expressed as shown in Equation 1 [103]. In this formulation,  $\vec{E}$  represents the electric field intensity in volts per meter (V/m),  $\epsilon_r$  is the relative permittivity of the material, and  $\mu_r$  denotes the relative permeability. The electrical conductivity,  $\sigma$ , is defined as  $\sigma = 2\pi f \epsilon_0 \epsilon''$ , where  $\epsilon''$  is the imaginary part of the permittivity and  $\epsilon_0$  is the permittivity of free space, equal to  $8.854 \times 10^{-12}$  F/m. The wave number,  $k_0$ , is given by  $k_0 = \frac{\omega}{c}$ , with  $\omega$  representing the angular frequency and  $c$  being the speed of light in vacuum ( $3 \times 10^8$  m/s). This equation provides the foundation for determining how the electric field propagates, interacts with the material, and dissipates energy through dielectric losses.

$$\nabla \times \frac{1}{\mu_r} (\nabla \times \vec{E}) - k_0^2 \left( \epsilon_r - \frac{\sigma}{\omega \epsilon_0} j \right) \vec{E} = 0$$

1

In most microwave applications and experimental practices [104-111], the strength of the applied electric field remains well below the fundamental atomic field threshold,  $E_{at} = 5.14 \times 10^{11}$  V/m

[112, 113]. Under these conditions, the contribution of magnetic losses to the overall energy dissipation is negligible. Consequently, the resistive power loss within the material is dominated entirely by dielectric losses. This simplification allows the modeling of microwave heating to focus solely on dielectric effects without significant error.

The relative permittivity of a material,  $\epsilon_r$ , describes its ability to store and dissipate electrical energy when exposed to an oscillating electric field, and is expressed as  $\epsilon_r = \frac{\epsilon}{\epsilon_0} = \epsilon' - \epsilon''j$ . In this formulation,  $\epsilon'$  represents the real part, often referred to as the relative dielectric constant, which quantifies the material's capacity to store electrical energy. The imaginary part,  $\epsilon''$ , is known as the relative dielectric loss and characterizes the material's ability to dissipate energy as heat due to dielectric relaxation processes. Together, these components fully describe the dielectric behavior of the material under microwave irradiation. It might worth mentioning that, conventionally, the choice of sign preceding the imaginary part,  $\epsilon''$ , is arbitrary and indicates how the field frequency dependency is defined. Defining field frequency dependency with a minus sign i.e.,  $E = E_0 e^{-i\omega t}$ , then a negative sign precedes the imaginary part,  $\epsilon = \epsilon' - i\epsilon''$ .

The volumetric thermal power generated as a result of dielectric interactions within the material, denoted by  $Q$  (W/m<sup>3</sup>), can be calculated using the expression provided in Equation 2 [114, 115]. This quantity represents the rate at which electromagnetic energy is converted into heat inside the material due to its dielectric properties.

$$Q = 2\pi\epsilon_0\epsilon''f|\vec{E}|^2$$

The spatial distribution and subsequent dissipation of the thermal power generated within the material ( $Q$ ) are described using Fourier's heat conduction equation, as presented in Equation 3 [116]. In this equation,  $T$  denotes the temperature in kelvins (K),  $k$  represents the thermal

conductivity in W/m.K,  $C'_p$  is the apparent specific heat capacity in J/kg.K, and  $\rho$  is the material density in kg/m<sup>3</sup>. This formulation accounts for the transfer of heat within the material, enabling the prediction of temperature evolution resulting from dielectric heating under microwave exposure.

$$\frac{\partial T}{\partial t} = \frac{k}{\rho C'_p} \nabla^2 T + \frac{Q}{\rho C'_p} \quad 3$$

An apparent heat capacity approach ( $C'_p$ ) was employed to account for the energy associated with the latent heat of evaporation [117]. This approach is expressed as  $C'_p = C_p + C_L$ . In this expression,  $C_p$  represents the equivalent heat capacity of the material mixture, calculated as  $C_p = \sum_{n=1}^2 C_{p,n} \theta_n$ , where  $C_{p,n}$  is the specific heat capacity of phase  $n$  (wet or dry), and  $\theta_n$  is the corresponding mass fraction. The term  $C_L$ , given in Equation 4, is used to approximate the distribution of latent heat required for evaporation, applied incrementally over a defined temperature interval  $\Delta T = T_2 - T_1$ . Within this interval,  $\lambda$  denotes the latent heat of water, and  $T_{1\rightarrow 2}$  represents the midpoint of the phase change range. This method allows the inclusion of phase change effects in the heat transfer model without explicitly solving separate energy equations for evaporation, thereby simplifying numerical computations while maintaining accuracy in predicting temperature evolution during drying. The wet phase linearly varies from 1 to 0 toward the dry phase over the defined temperature interval  $\Delta T = T_2 - T_1$ .

$$C_L(T) = \begin{cases} 0 & T < T_1 \\ \frac{2\lambda}{T_{1\rightarrow 2} - T_1} \cdot \frac{T - T_1}{T_2 - T_1} & T_1 \leq T < T_{1\rightarrow 2} \\ \frac{2\lambda}{T_2 - T_{1\rightarrow 2}} \cdot \frac{T_2 - T}{T_2 - T_1} & T_{1\rightarrow 2} \leq T \leq T_2 \\ 0 & T > T_2 \end{cases} \quad 4$$

To model the effect of forced convective cooling ( $q$ ) on the lateral surfaces of the sample ( $A$ ) due to air inflow in the microwave cavity, a convective boundary condition was applied in the heat transfer simulations. The heat flux per unit area was expressed as  $\frac{q}{A} = U(T_{ext} - T)$ , where  $T_{ext}$  is the temperature of the cavity air, maintained at 19.8 °C, and  $T$  represents the temperature at points on the sample surface. The overall convective heat transfer coefficient,  $U$ , was computed as  $U = 1/\left[\frac{1}{h_{air}} + \frac{\delta_{glass}}{k_{glass}}\right]$ . Here,  $h_{air}$  is the convective coefficient of air, determined using empirical correlations [116], specifically  $Nu = 0.037Re^{\frac{4}{5}}Pr^{\frac{1}{3}}$ , where  $Nu$  is the Nusselt number,  $Re$  is the Reynolds number, and  $Pr$  is the Prandtl number.  $\delta_{glass}$  and  $k_{glass}$  denote the thickness (5 mm) and thermal conductivity (1.143 W/m·K) of the Pyrex glass plate supporting the samples [118]. The resulting values of  $U$ , presented in **Table 3.4**, showed strong agreement with both the experimental findings of Halder and Datta [119] for similar conditions and with established empirical correlations [120].

**Table 3.4** The calculated values of forced convection coefficient applied to lateral surfaces of the sample.

Surface	Dimensions (m × m)	Pr <sup>1</sup>	Re	$U$ (W/m <sup>2</sup> .K)
Top surface <sup>2</sup>	0.126 × 0.086		26513	34.1
Lateral short surfaces	0.086 × 0.014	0.71	38845	34.1
Lateral long surfaces	0.126 × 0.014		26513	31.6

<sup>1</sup> The following properties are considered for ambient air; temperature = 19.8 (°C), dynamic viscosity =  $81.6 \times 10^{-7}$  Pa.s, specific heat capacity = 1005 J/kg.K, and thermal conductivity = 0.0257 W/m.k

<sup>2</sup> As the top surface is directly exposed to air, the term  $\delta_{glass}/k_{glass}$  is excluded from the calculation of  $U$ .

In the numerical model, the post-exposure thermal response of the samples was simulated by applying a convective cooling boundary over the handling time for all lateral surfaces. A similar convective coefficient, [ $U \leq 50 \text{ W/m}^2 \cdot \text{K}$ ], was used under free-stream conditions to realistically replicate the heat loss during sample transfer [119].

### 3.3.2 Initial and Boundary Conditions

In the heat transfer model, the bottom layer of sample domain is assumed isothermal without any energy exchange with the ceramic plate. The remaining surfaces exchange energy due to convection with the air in the cavity driven by air inflow. Since there is no dielectric loss in air and ceramic plate domains, the heat transfer is only considered in sample domain. In the electromagnetic model, all the internal surfaces of cavity and waveguide, together with the lateral surfaces of stirrers are assumed as perfect electrical conductors.

### 3.3.3 Numerical Stability Considerations

To verify the accuracy of the numerical simulations and confirm mesh independence in both the electromagnetic and heat transfer models, specific convergence criteria were established.

For the electromagnetic model, the primary metric was the total resistive power loss within the material volume, while for the heat transfer model, the power balance across all boundaries was used. The total resistive power loss, expressed in watts (W), was calculated by integrating the local volumetric power generation  $Q$  (from Eq. 3) over the entire volume of the sample i.e.  $Q_s = \int Q dV$ .

This integration provides a global measure of energy dissipation due to dielectric heating.

For the heat transfer analysis, the power balance parameter ( $E_{HT}$ ) was defined as in Eq. (5) [100].

This parameter quantifies the difference between the energy entering and leaving the system,

ensuring that the numerical solution conserves energy across the computational boundaries. Both metrics served as essential indicators of convergence, ensuring that further mesh refinement would not significantly affect the accuracy of the results.

$$E_{HT} = \frac{\left| Q_s - \frac{d}{dt} \int \rho E dV - \int q_s dS \right|}{Q_s} \quad 5$$

In Eq. (5), the term  $\int q_s dS$  represents the total power exchanged through the boundaries of the material due to convective cooling. Here,  $q_s$  denotes the convective heat flux per unit area (i.e.,  $q_s = q/A$ , as defined earlier in Eq. 5), and  $S$  refers to the surface over which the exchange occurs.

The second term,  $\frac{d}{dt} \int \rho E dV$  accounts for the temporal rate of change of the material's specific internal energy, integrated over the entire volume  $V$ . This term incorporates both sensible heat (energy change due to temperature variation) and latent heat (energy change due to phase transformation such as evaporation). Here,  $E$  is the specific internal energy expressed in joules per kilogram (J/kg), and  $\rho$  is the local material density. Together, these terms ensure that the heat transfer model satisfies the principle of energy conservation by balancing convective losses with internal energy changes over time.

Within the electromagnetic model, the determination of mesh size was guided by the Nyquist Criterion, which dictates that the largest allowable mesh element size ( $h_{\max}$ ) must be substantially smaller than half the wavelength ( $\lambda$ ) of the electromagnetic wave propagating through the medium.

This requirement, expressed as  $h_{\max} \ll \frac{\lambda}{2} = \frac{1}{2} \frac{c}{f \sqrt{\epsilon' \mu'}}$ , ensures sufficient resolution for accurately capturing the spatial variations of the harmonic electromagnetic fields [121]. In practical terms, this criterion prevents aliasing and numerical dispersion errors, which could otherwise compromise the fidelity of the simulation results. To comply with established best practices

reported in the literature [122], the present study adopted a discretization strategy employing at least six nodes per  $h_{\max}$ . This choice provides a robust balance between computational efficiency and solution precision, ensuring that the modeled electromagnetic field distribution remains reliable throughout the simulation domain.

In the heat transfer modeling framework, an implicit numerical scheme based on the backward Euler method was employed. This approach inherently guarantees numerical stability, meaning the Courant–Friedrichs–Lowy (CFL) condition does not impose restrictions on the timestep size [123], and therefore there is no strict upper bound for the timestep [124]. Nevertheless, since both the mass matrix ( $\mathbf{M}$ ) and stiffness matrix ( $\mathbf{K}$ ) depend on thermal conductivity and apparent heat capacity — which themselves vary with moisture content — this dependency can cause the resulting system of equations to become ill-conditioned [125, 126]. Ill-conditioning can significantly reduce numerical accuracy and convergence efficiency. To address this, COMSOL Multiphysics [100] integrates a pseudo time-stepping strategy, wherein the timestep size is adaptively controlled based on the system's properties. Specifically, the timestep  $dt$  is constrained according to the largest eigenvalue ( $\gamma_{\max}$ ) of the matrix  $\mathbf{M}^{-1}\mathbf{K}$ , as expressed by  $dt \leq \frac{2}{\gamma_{\max}}$ . This approach ensures that the simulation remains both stable and sufficiently accurate, despite the variations in material properties caused by moisture changes.

Through systematic mesh refinement studies, it was determined that element sizes of approximately 5 mm provided stable and reliable numerical results, balancing computational efficiency with numerical accuracy (**Figure 3.7**). Further reduction in element size produced negligible changes in the key convergence indicators, confirming numerical consistency and mesh

independency. Specifically, variations in the total resistive power loss were smaller than 5 W, while deviations in the heat transfer power balance remained under 1% (**Figure 3.6**).

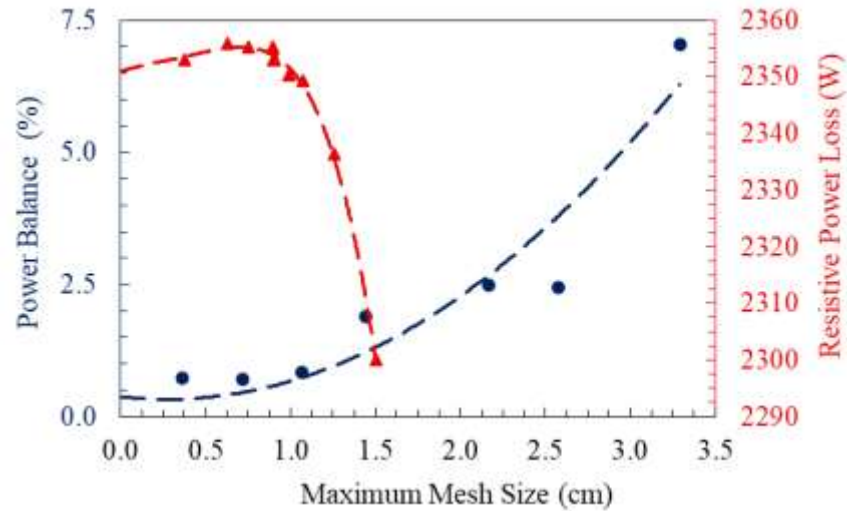


**Figure 3.6** Mesh dependency analysis of resistive power loss and heat power balance with dashed trendlines.

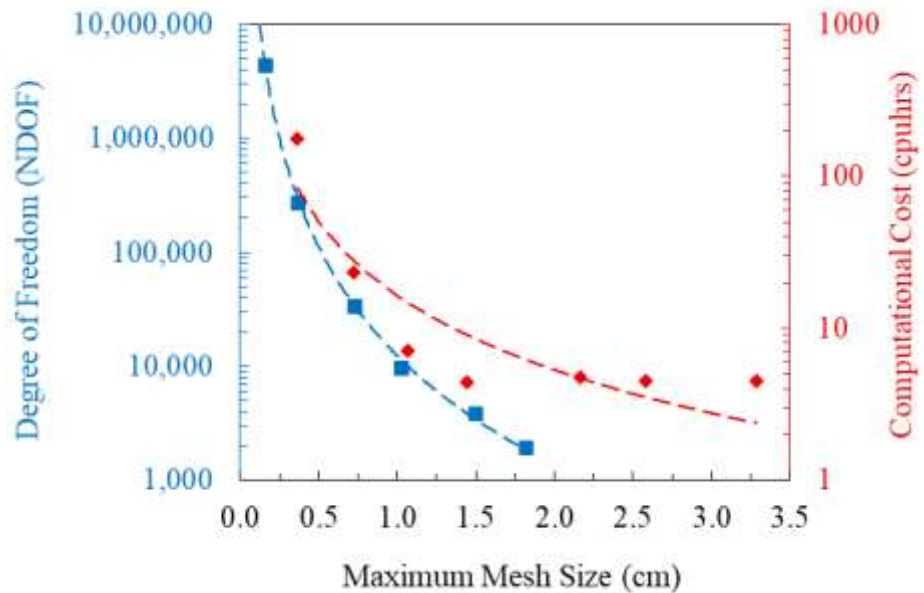


**Figure 3.7** The number of elements (degree of freedom) generated with mesh refinement and their respective computational costs (measured for ten consecutive iterations), with dashed trendlines.

In **Figure 3.8**, the improvement in numerical accuracy resulting from successive mesh refinements was evaluated using an  $h$ -convergence analysis [127, 128], expressed by the relation  $\epsilon = Ch^r$ , where  $\epsilon$  represents the normalized convergence error at a given mesh size, calculated relative to the finest mesh tested across all cases [129]. The parameter  $r$  denotes the convergence rate, while  $C$  is a constant specific to the physical model under consideration. Consistent with theoretical expectations [127], the heat transfer model, which employed linear finite elements, exhibited a convergence rate of approximately 0.98 (close to unity), confirming the reliability of the discretization scheme. Similarly, the electromagnetic model—discretized using quadratic elements—demonstrated a convergence rate of 1.85 (approaching 2), in agreement with anticipated results. These findings validate both models' numerical accuracy and their adherence to established convergence behavior for their respective element orders.

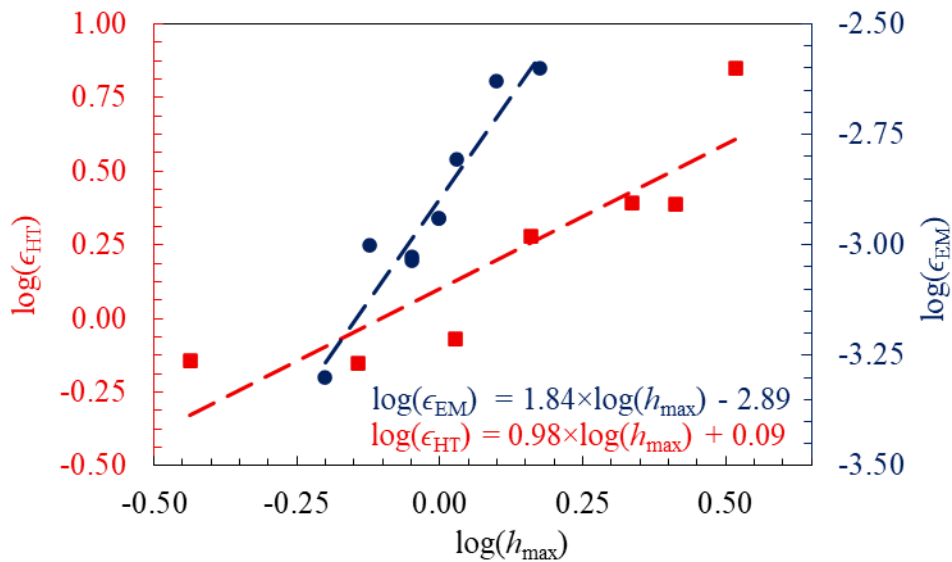


**Figure 3.8** The  $h$ -convergence analysis for electromagnetic and heat transfer meshes, illustrating error reduction with mesh refinement.

### 3.3.4 Model Implementation

The developed computational model incorporated coupled electromagnetic and heat transfer modules within COMSOL Multiphysics [100]. A numerical representation of the microwave oven was constructed according to the geometric dimensions and operational parameters provided by the manufacturer as shown in **Figure 3.9**. Electromagnetic properties were defined as  $\varepsilon_{r,\text{air}} = \mu_{r,\text{air}} = 1$  for air [130], and  $\varepsilon_{r,\text{ceramic}} = 38$ ,  $\mu_{r,\text{ceramic}} = 1$  for ceramic [131]. The experimentally characterized dielectric properties, thermal conductivity, apparent specific heat capacity, and density of the sample were implemented as functions dependent on moisture content [14].

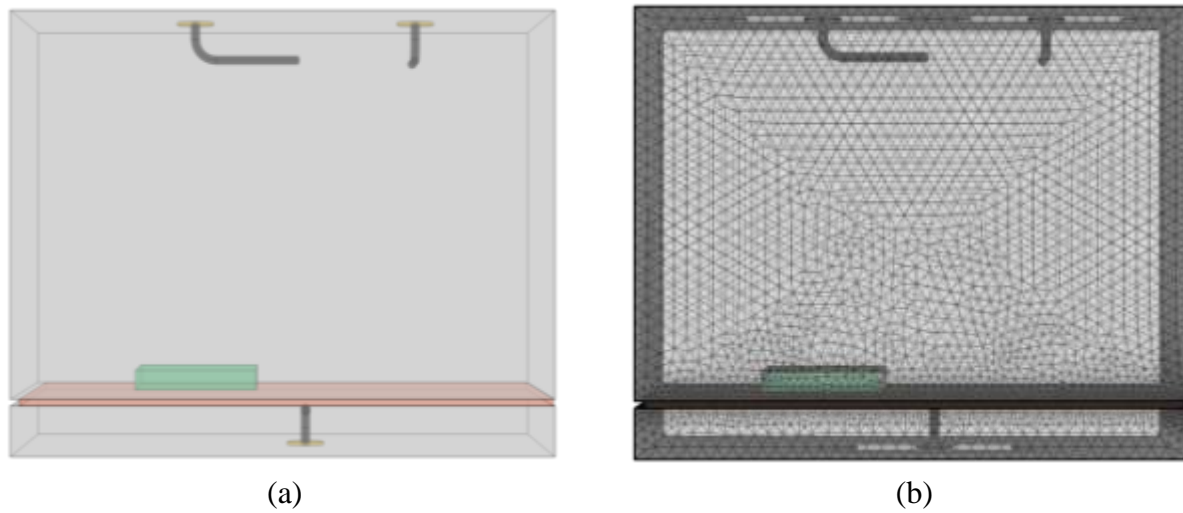


**Figure 3.9** Schematic representation of the modelled microwave oven illustrating: (a) its components including mode stirrers (highlighted in yellow), the ceramic support plate (highlighted in red), and the sample (highlighted in green); and (b) the finite element mesh used for electromagnetic and heat transfer simulations.

For the discretization, quadratic tetrahedral elements (10-node) were used for the electromagnetic model, while linear tetrahedral elements (4-node) were adopted for the heat transfer calculations [100]. The electromagnetic field equations were solved using a Generalized Minimal Residual Method (GMRES) iterative solver, whereas the temperature field was computed via the Parallel

Direct Solver (PARDISO) [100]. This combination ensured efficient and accurate coupling of the electromagnetic and thermal simulations within the model framework.

### 3.3.5 The Quasi-Transient Approach in Solving the Coupled Model

To reduce the computational expense associated with simulating the fully transient rotation of the mode stirrers, a quasi-transient approach was implemented. This method involved discretizing a full revolution (cycle) of the stirrers into incremental angular steps [132], thereby significantly reducing model size and computational cost. Within this loosely coupled sequential modelling scheme, the electromagnetic and temperature fields were still solved iteratively and bidirectionally [100].

To determine an appropriate angular increment for stirrer repositioning, the electromagnetic field was computed for various angular increments over a complete revolution (corresponding to 3.5 s) at an initial temperature of 20 °C. Variations in resistive power loss were then evaluated. Since the dielectric properties of the material remain effectively constant above moisture contents of 10%, any changes in resistive power loss in this scenario could be attributed solely to the stirrers' angular positioning. The results, presented in **Figure 3.10**, indicate that an angular increment of 45° is sufficient to accurately capture variations in resistive power loss caused by stirrer rotation. Consequently, the stirrers' positions were incrementally updated every 0.4375 s, consistent with the measured angular velocity of  $1.795 \text{ rad. s}^{-1}$ .

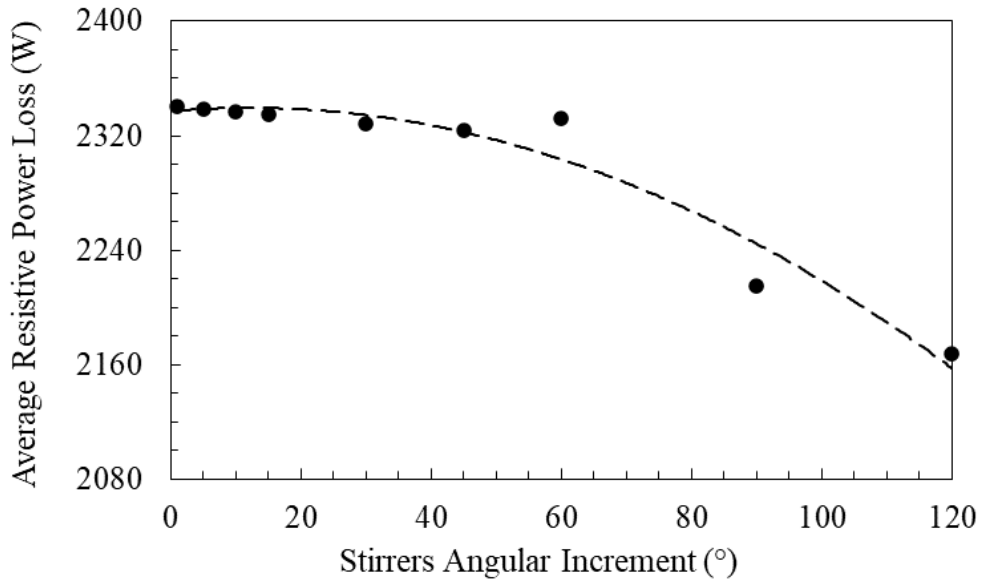


**Figure 3.10** Convergence of power loss averaged over discrete angular positions for a single revolution.

## 3.4 Results and Discussion

### 3.4.1 Experimental Mass Loss and Temperature

**Table 3.5** presents the variations in average surface temperature and water loss observed at different microwave dosages, with exposure times ranging from 12 to 60 s (Cases I–V). The total amount of evaporated water increased with longer microwave exposures and higher energy dosages. At lower energy levels, the supplied energy was insufficient to initiate significant evaporation and was therefore predominantly absorbed as sensible heat, resulting in a marked increase in material temperature. As energy input increased, the water extraction rate [14] rose correspondingly, eventually reaching a plateau at approximately 0.25 gram per kW.hr/t, indicating that evaporation became the dominant mechanism of energy consumption at higher dosages. This gradual shift from sensible heating to latent heat absorption led to diminishing

variations in average surface temperature, with average surface temperatures stabilizing near 80 °C at the highest dosages tested.

**Table 3.5** Measured surface temperature and water removed at each microwave dosage.

Case	Time-in-Oven (s)	Energy Dosage (kW. hr/t)	Temperature (°C)	Water Loss (g)	Water Extraction Rate (g per kW. hr/t)
I	12	25.89	52.5	1.36	0.05
II	15	34.98	62.8	2.71	0.08
III	30	80.44	79.9	12.82	0.16
IV	45	125.89	81.6	27.50	0.22
V	60	171.35	84.3	40.08	0.23

### 3.4.2 Effect of Phase Change Interval

The influence of the prescribed phase change interval ( $\Delta T$ ) on the numerical prediction of evaporation was systematically evaluated [88, 133, 134], with the results presented in **Table 3.6** for Cases I, III, and V. A broader phase change interval leads to smaller predicted mass losses, as the latent heat is allocated more gradually across the material domain. This results in a wider distribution of thermal energy, delaying the onset of evaporation. Conversely, a narrower phase change interval concentrates the release of latent heat, thereby increasing predicted mass loss.

As  $\Delta T$  decreases, the predicted mass losses converge asymptotically. However, sharper transitions tend to introduce numerical instability, requiring the solver to adopt significantly smaller time steps [135], which markedly increases computational cost. While smaller phase change intervals more closely represent the physical evaporation process, the difference in predicted mass losses

between intervals of  $\Delta T \leq 1$  °C and 2.5 °C was found to be negligible. Therefore, a phase change interval of 2.5 °C was adopted in this study, offering a balanced compromise between numerical accuracy and computational efficiency.

**Table 3.6** The effect of prescribed phase change interval on predicted mass loss.

	Water Loss (g)		
Energy Dosage (kW. hr/t)	25.89 (I)	80.44 (III)	171.35 (V)
$\Delta T$ (°C)			
1	1.19	18.65	43.46
2.5	1.07	18.08	43.33
5	0.53	15.30	41.51
10	0.38	13.71	36.09

### 3.4.3 Effect of Thermal Conductivity

The thermal conductivity of the solid phase carries an experimental uncertainty of  $\pm 10\%$ , which directly contributes to uncertainty in the estimated overall thermal conductivity. The impact of this variability on predicted mass loss across different energy dosages is presented in **Figure 3.11**. These predictions are compared with experimental measurements of mass loss, where the associated uncertainty range accounts for potential errors in mass loss quantification, including weighing precision and sample handling.

The results indicate that a higher (overestimated) thermal conductivity enhances thermal energy dissipation, producing a more uniform temperature distribution within the material. This effect

reduces local overheating and consequently leads to underestimation of water loss predictions for the same microwave energy input. Conversely, a lower (underestimated) thermal conductivity restricts heat diffusion, causing localized temperature accumulation and thereby overestimating evaporation rates.

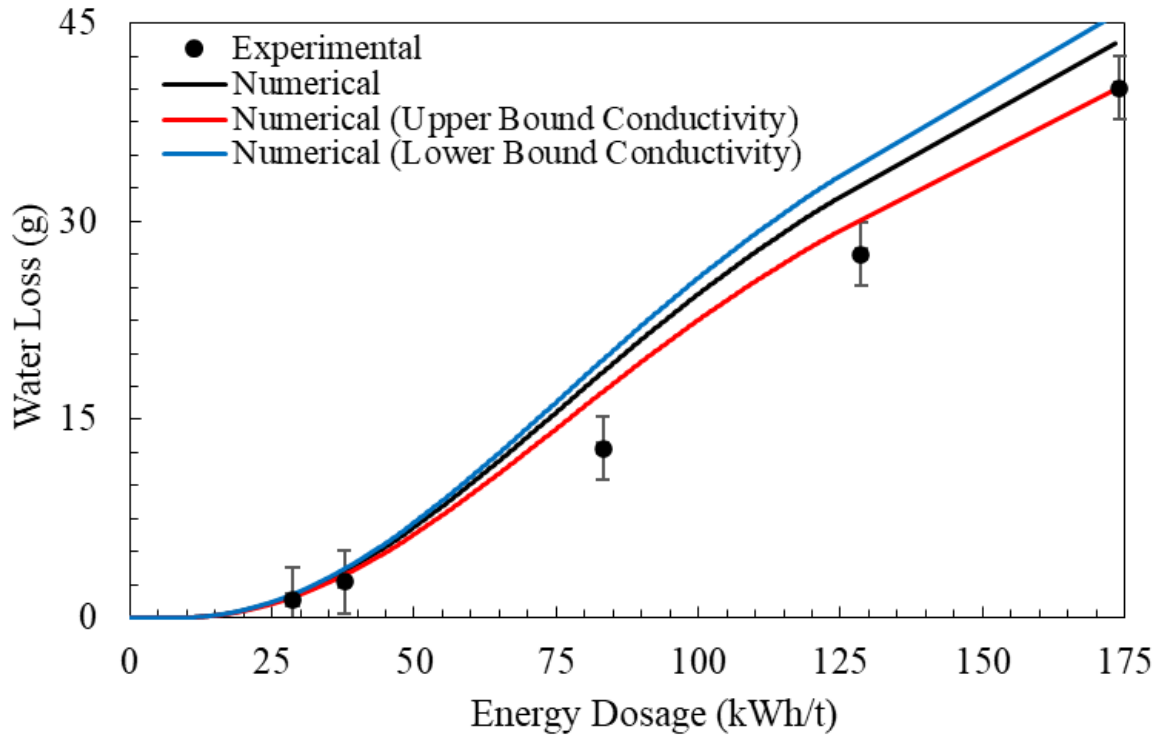


**Figure 3.11** Dependency of numerical results for evaporation on the thermal conductivity (with  $\Delta T = 2.5 \text{ } ^\circ\text{C}$ ).

**Figure 3.12** illustrates the shortcomings of the widely used arithmetic mean model in predicting mass loss during drying. A substantial discrepancy is evident between the predictions generated using the arithmetic mean model and the corresponding experimental data. This deviation is markedly greater than the results obtained when employing the recommended thermal conductivity model, as shown in **Figure 3.11**. The arithmetic mean model consistently overestimates mass loss, a discrepancy that originates from its underestimation of the actual thermal conductivity of the

material mixture. Consequently, this model predicts the onset of evaporation significantly earlier than observed experimentally. These findings reaffirm the critical importance of selecting an appropriate thermal conductivity mixture model, a point emphasized in prior research [84-88]. Failure to adopt a suitable model can lead to significant errors in predicting drying behavior, potentially undermining the accuracy and reliability of numerical simulations in mineral processing applications.

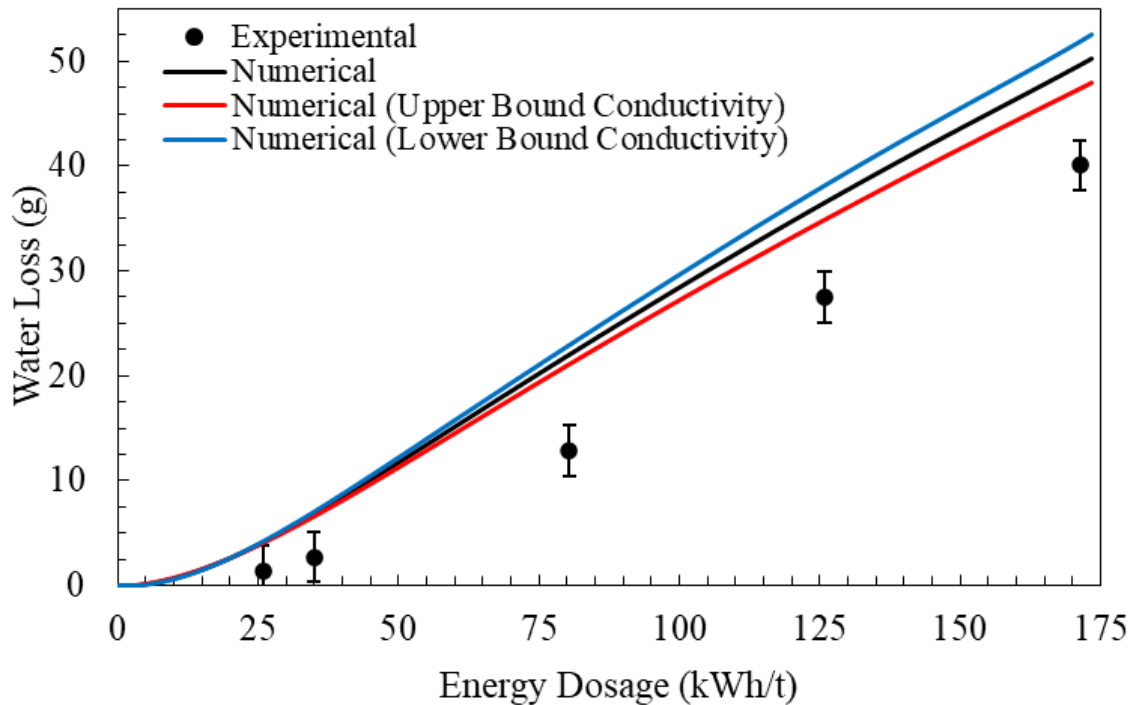


**Figure 3.12** Failure of arithmetic mean thermal conductivity model in prediction of evaporation (with  $\Delta T = 2.5 \text{ }^{\circ}\text{C}$ ).

#### 3.4.4 Surface Temperature Profiles: Experimental vs. Numerical

The change in average surface temperatures, captured using an infrared (IR) camera, is compared with numerical model predictions in **Figure 3.13**. The error bars represent the range of uncertainty arising from potential sources such as IR camera precision, image processing, and post-exposure sample handling. In the simulations, solid and dashed lines denote the exposure stage (microwave

heating) and the post-exposure stage (cooling during handling time), respectively. The results demonstrate excellent agreement between numerical model predictions and experimental measurements for single-shot microwave experiments. For high energy dosages (above 100 kW·hr/t), applying an overall heat transfer coefficient of  $U = 50 \text{ W/m}^2 \cdot \text{K}$  resulted in an absolute relative deviation ( $ARD = |T^{\exp} - T^{\text{num}}|/T^{\exp}$ ) of less than 10% between predicted ( $T^{\text{num}}$ ) and measured ( $T^{\exp}$ ) surface temperatures. At lower energy dosages, using  $U = 25 \text{ W/m}^2 \cdot \text{K}$  improved agreement, producing an ARD below 5%.

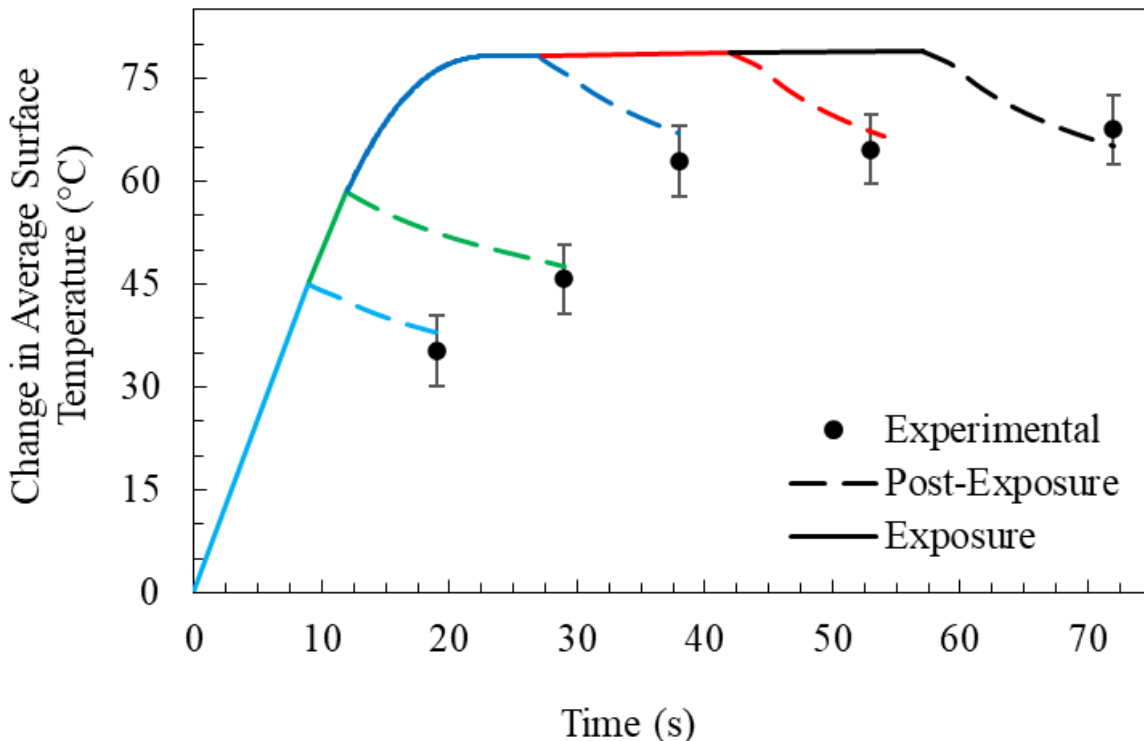
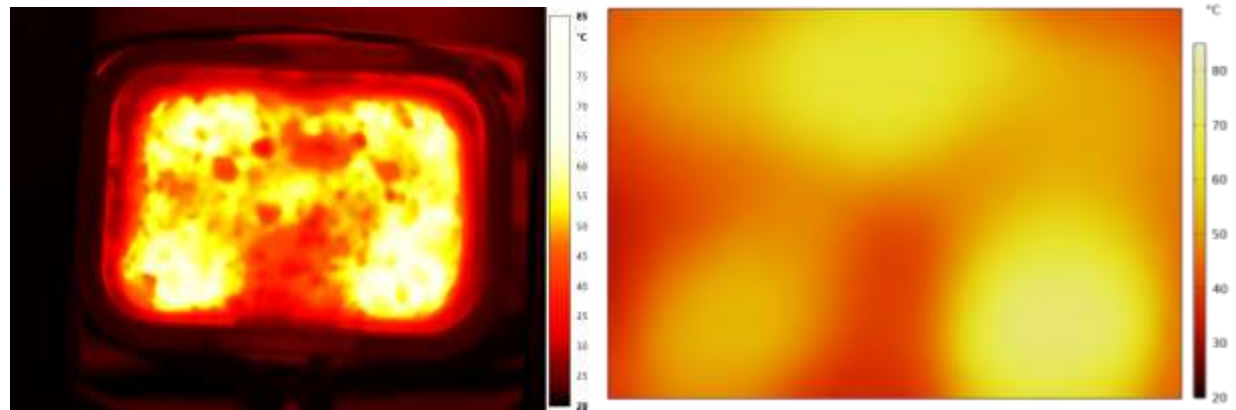


**Figure 3.13** Comparison of the average surface temperature recorded by an IR Camera with numerical model predictions for Cases I through V. Numerical results for  $\Delta T = 2.5 \text{ } ^\circ\text{C}$  and  $k_s = 1.79 \text{ W/m.K}$ .

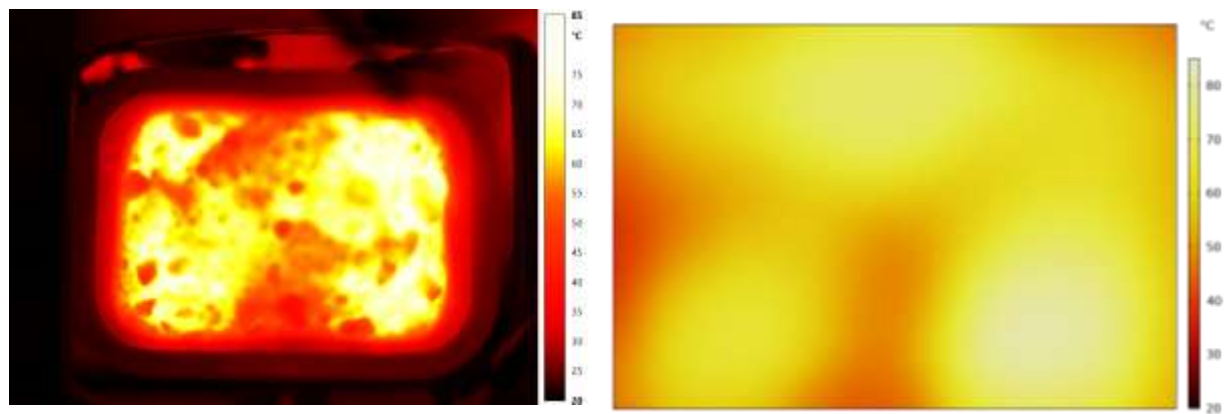
**Figure 3.14** presents the surface temperature profiles obtained from infrared (IR) imaging alongside the corresponding predictions from the numerical model for Cases I through III. **Table 3.7** provides a quantitative comparison of the surface temperature fields, including extreme values, mean temperature, and standard deviation. The comparison between experimental and numerical profiles demonstrates strong overall agreement. It should be noted that the numerical model does not account for the particulate or granular nature of the material, which likely contributes to the localized hot and cold spots observed in the IR images. Incorporating such microstructural heterogeneities could further improve the model's capability to capture spatial temperature variations with higher accuracy [136]. Nonetheless, the present model exhibits satisfactory agreement with the experimental results.

**Table 3.7** Surface temperature measured using IR camera thermal imaging, with corresponding numerical predictions (in parenthesis).

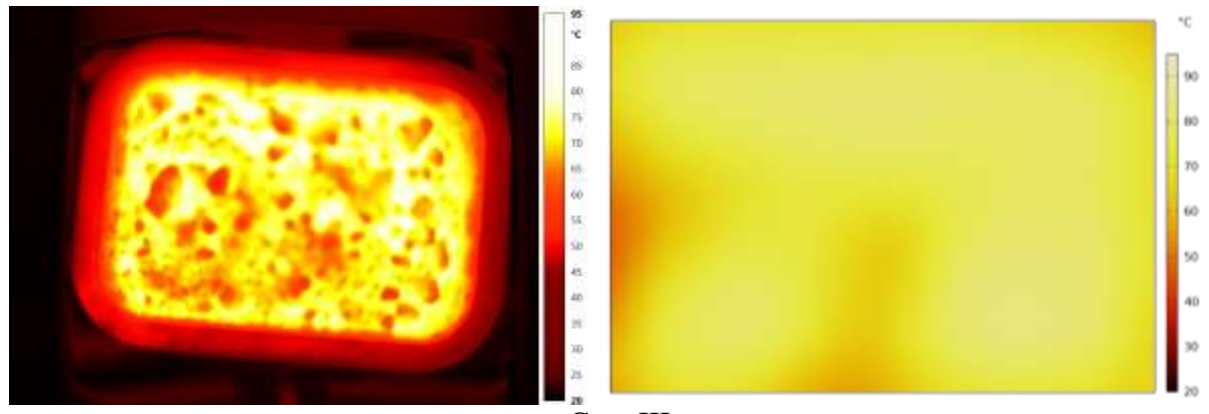
Case	Surface Temperature (°C):			Standard Deviation (°C), $\sigma$ :
	Experimental (Numerical)		Average	
	Maximum	Minimum		Experimental (Numerical)
I	85.0 (78.9)	28.3 (31.6)	52.5 (54.4)	9.6 (9.1)
II	84.4 (83.2)	35.7 (39.2)	62.8 (64.4)	9.1 (8.2)
III	97.0 (98.3)	61.1 (65.7)	79.9 (85.5)	4.8 (8.1)
IV	102.8 (98.6)	62.2 (66.0)	81.6 (85.6)	4.9 (8.2)
V	103.7 (98.8)	62.7 (66.4)	84.3 (86.1)	5.8 (7.9)



Case I



Case II



Case III

**Figure 3.14** Comparison of the surface temperature profiles captured by IR imaging (left) with numerical results (right) for Cases I through III.

### 3.4.5 Heating Uniformity Index

**Figure 3.15** presents the uniformity index ( $UI$ ) for Cases I through V. The Uniformity index is defined as  $UI = 1 - \sigma/\mu$ , where  $\sigma$  and  $\mu$  denote the standard deviation and mean of the surface temperature, respectively [137]. The standard deviation is defined as  $\sigma = \sqrt{\sum[T_i - \mu]^2/(N - 1)}$  where  $N$  is number of datapoints and  $T_i$  is the temperature at any given point. The mean is defined as  $\mu = \sum T_i/N$ . The experimental values of the  $UI$  remained above 80%, suggesting a high degree of temperature uniformity across the surface of the sample. This is attributed to the presence of stirrers [90, 91], which facilitates a more homogenous distribution of energy within the sample. As shown, the uniformity index increases with energy dosage (exposure time), with this effect becoming more pronounced at higher energy dosages due to enhanced thermal diffusion throughout the material.

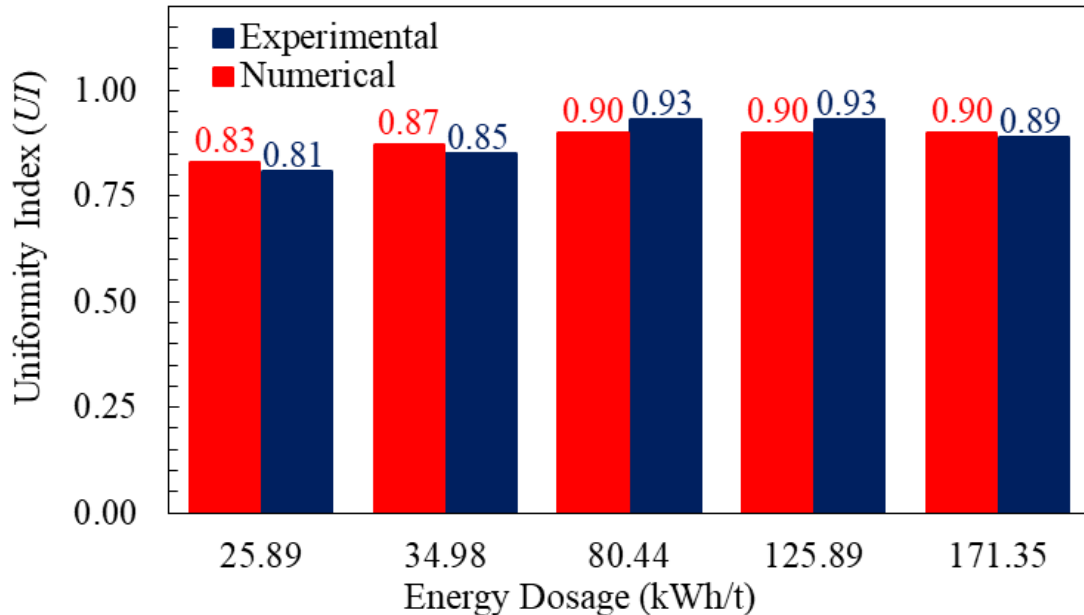


**Figure 3.15** Comparison of uniformity index for Cases I through V. Numerical results for  $\Delta T = 2.5$  °C and  $k_s = 1.79$  W/m. K.

### 3.4.6 Power Loss Profile

**Figure 3.16** illustrates the relationship between power loss, the angular orientation of the stirrers, and the moisture content of the samples. At the early stages of microwave exposure, fluctuations in power loss are largely influenced by the rotation of the stirrers, since variations in dielectric properties remain relatively insignificant when the moisture content is greater than 10%. As microwave treatment continues, a noticeable decline in power loss occurs in parallel with the gradual reduction in moisture content. This behavior can be explained by the strong sensitivity of dielectric properties to moisture levels; as water is removed, the dielectric response of the material weakens, leading to a progressive decrease in power absorption. The effect becomes particularly evident after approximately 30 seconds of irradiation, when the diminishing moisture content exerts a dominant influence on the overall energy dissipation within the sample.

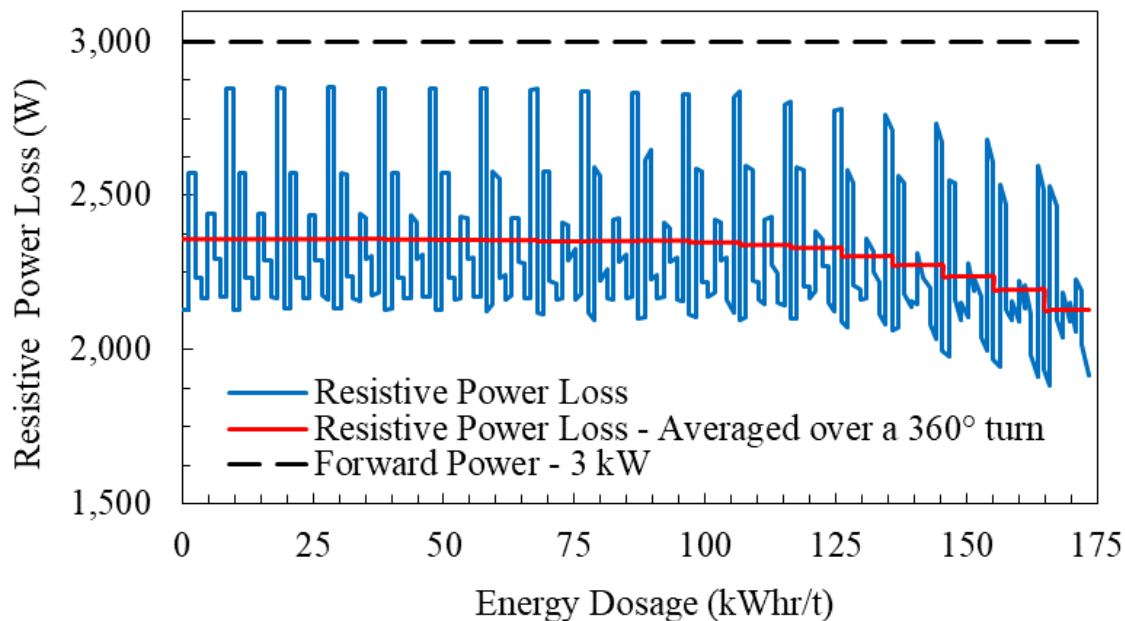


**Figure 3.16** The computed resistive power loss (Numerical results for  $\Delta T = 2.5 \text{ }^{\circ}\text{C}$  and  $k_s = 1.79 \text{ W/m.K}$ ).

### 3.4.7 Drying Efficiency

The most commonly used latent-only drying efficiency fails to account for energy expended on the heating up of the water content [138], which contributes to 13% of absorbed energy expenditure. This eventually can lead to misleading conclusions, particularly in drying of high moisture containing materials. Therefore, the drying efficiency ( $\eta_v$ ) is defined as the ratio of the net energy expended for heating the removed mass of water ( $m_v$ ) from its initial temperature ( $T_0$ ) to onset of evaporation (100 °C), and its subsequent evaporation to the total forward microwave energy, given as  $\eta_v = \frac{m_v C_{p,w} (100^\circ\text{C} - T_0) + m_v L_v}{P \times t}$ . Here,  $P$  is the microwave forward power (i.e., 3 kW), and  $t$  is the irradiation duration.

As illustrated in **Figure 3.17**, the efficiency curve begins to stabilize at energy dosages above 100 kW.hr/t (equivalent to exposure durations exceeding 30 seconds). This plateau behavior corresponds to the relatively minor variations observed in the rate of water removal at energy inputs beyond this threshold, as summarized in **Table 3.5**. At higher microwave energy inputs, a larger fraction of the sample is heated to temperatures sufficient to initiate evaporation. Nevertheless, the rate of moisture extraction is constrained by the kinetics of surface evaporation. Previous studies [14, 139] have confirmed that once the material reaches a state of equilibrium surface saturation, further increases in energy dosage do not significantly enhance water removal or overall drying performance. Consequently, supplying energy beyond this threshold is considered inefficient and should be avoided, as also advised in the literature [14].

Numerical modeling results predicted that complete removal of moisture could theoretically be achieved with a drying efficiency of approximately 72.05% when an energy dosage of 200 kW.hr/t is applied, corresponding to a microwave exposure time of 66.82 seconds. It should be

noted, however, that resistive power losses decrease at elevated energy dosages due to their dependence on the moisture content, which could lead to a reduction in actual drying efficiency compared to the trend presented in **Figure 3.17**. Despite this limitation, the drying process benefits from conductive heat transfer: regions that have already been fully dried remain at higher temperatures than moisture-rich zones, thereby transferring thermal energy to the wetter regions. This redistribution of heat enhances overall drying performance and helps explain the improved efficiency observed at extended exposure times.

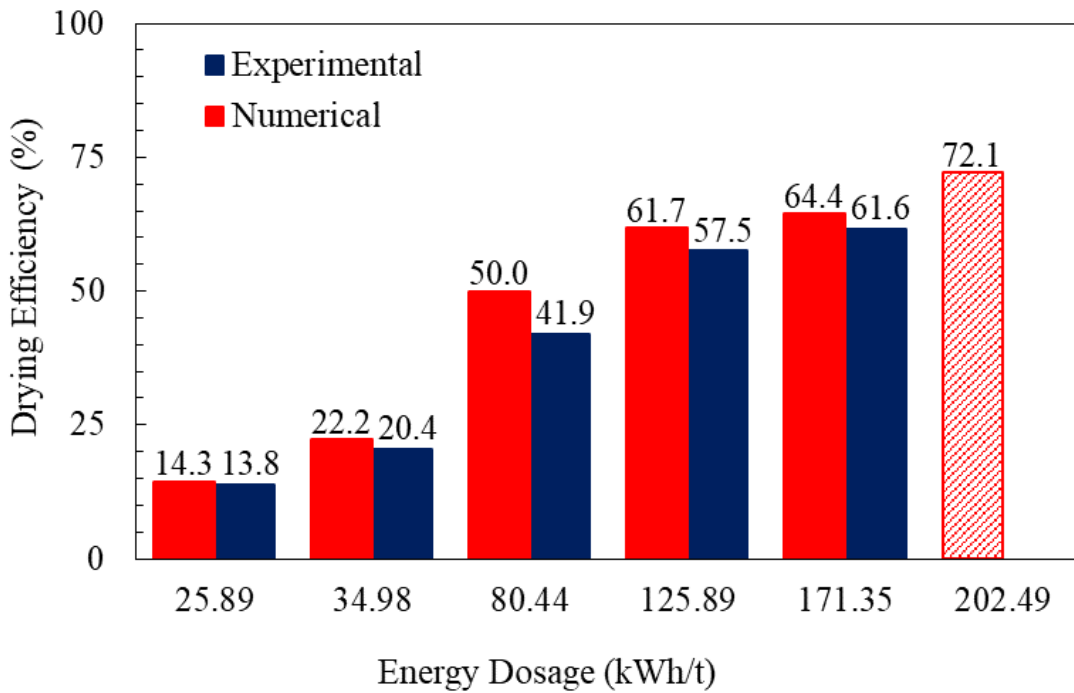


**Figure 3.17** Comparing the experimental and numerical drying efficiency. Numerical results for  $\Delta T = 2.5 \text{ }^{\circ}\text{C}$  and

$$k_s = 1.79 \text{ W/m.K.}$$

### 3.4.8 Heat Over Microwave Efficiency (HOME)

The heat over microwave efficiency (HOME) [140] is defined as the ratio of the microwave energy absorbed by the material (and expended on both overall sensible heat and latent energy) to the total forward microwave energy, and is given as  $\text{HOME} = \frac{Q_s - \int q_s dS}{P}$ . Variations in HOME are shown in

**Figure 3.18.**

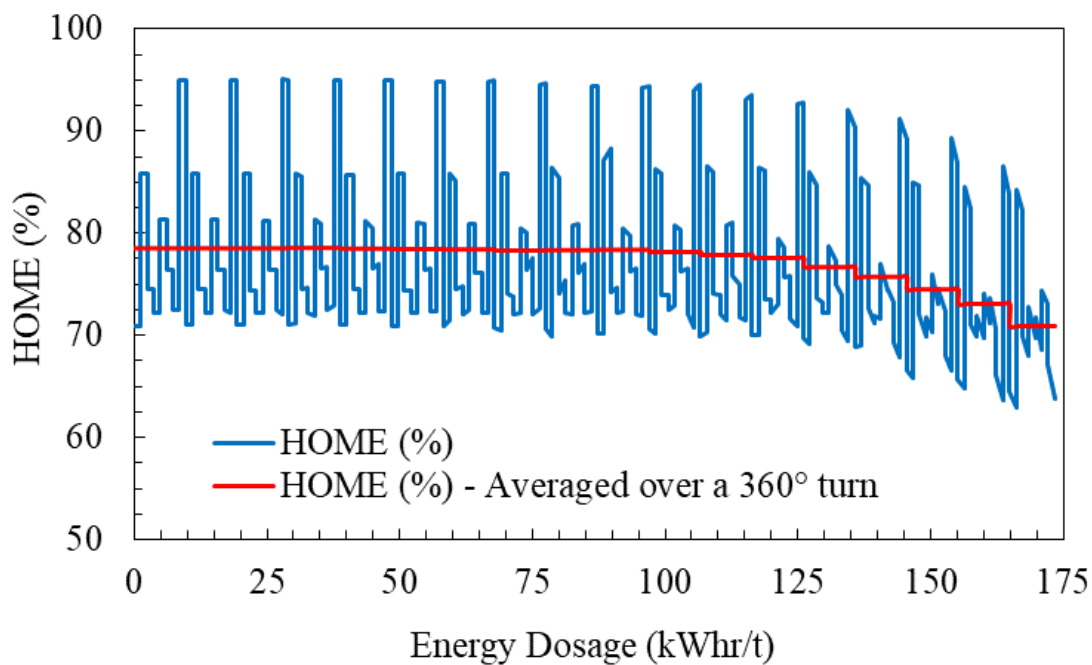


**Figure 3.18** The computed heat over microwave efficiency (Numerical results for phase change interval  $\Delta T = 2.5$  °C

and  $k_s = 1.79$  W/m. K).

The observed variations in HOME, as illustrated in **Figure 3.18**, can be attributed to two primary factors: (i) the dependence of power dissipation on both the moisture content of the material and the angular orientation of the microwave stirrers, and (ii) thermal energy losses caused by convection. During the initial stages of irradiation, fluctuations in HOME are largely governed by the rotation of the stirrers, which alters the distribution of microwave energy within the cavity. As

exposure time increases, a gradual decline in HOME is recorded, closely linked to the reduction in moisture content. Because power absorption is strongly influenced by the dielectric properties of water, the progressive loss of moisture leads to a corresponding decrease in energy uptake [74]. This downward trend becomes particularly evident after approximately 30 seconds of irradiation, when elevated rates of moisture removal accelerate the decline in HOME. At extended exposure times, the metric was observed to decrease by nearly 10% compared with shorter exposures. Furthermore, under higher energy dosages, the surface of the material reached substantially higher temperatures than under lower dosages. This temperature rise intensified convective heat transfer between the hot sample surface and the cooler ambient air within the cavity, potentially increasing thermal energy losses [95]. Despite this effect, the contribution of convective cooling was determined to be minimal, indicating that the majority of the absorbed microwave energy was directed toward sensible heating of the solid matrix and the latent heat required for water phase change.

### **3.4.9 Industry-recommended Maximum Temperature Threshold**

Numerical simulations were performed to evaluate the maximum internal temperatures of the material volume at varying microwave energy dosages immediately following irradiation, with reference to the industry-recommended critical temperature limit of 120 °C, as presented in **Figure 3.19** and **Figure 3.20**.

Across all tested dosages, the predicted peak temperatures remained safely below this threshold. This outcome confirms that the applied microwave heating conditions did not surpass the thermal limit that could otherwise impair the smelting performance or alter the metallurgical characteristics of the material. Consequently, the drying process was achieved without compromising

downstream processing efficiency, highlighting the potential suitability of microwave-based heating within practical operational constraints.

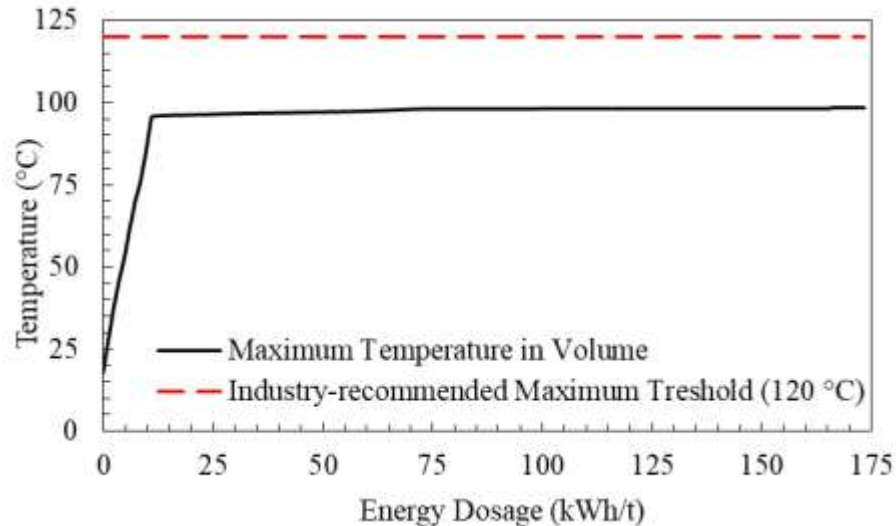


**Figure 3.19** Maximum volume temperatures. Numerical results for  $\Delta T = 2.5 \text{ }^{\circ}\text{C}$  and  $k_s = 1.79 \text{ W/m.K}$ .

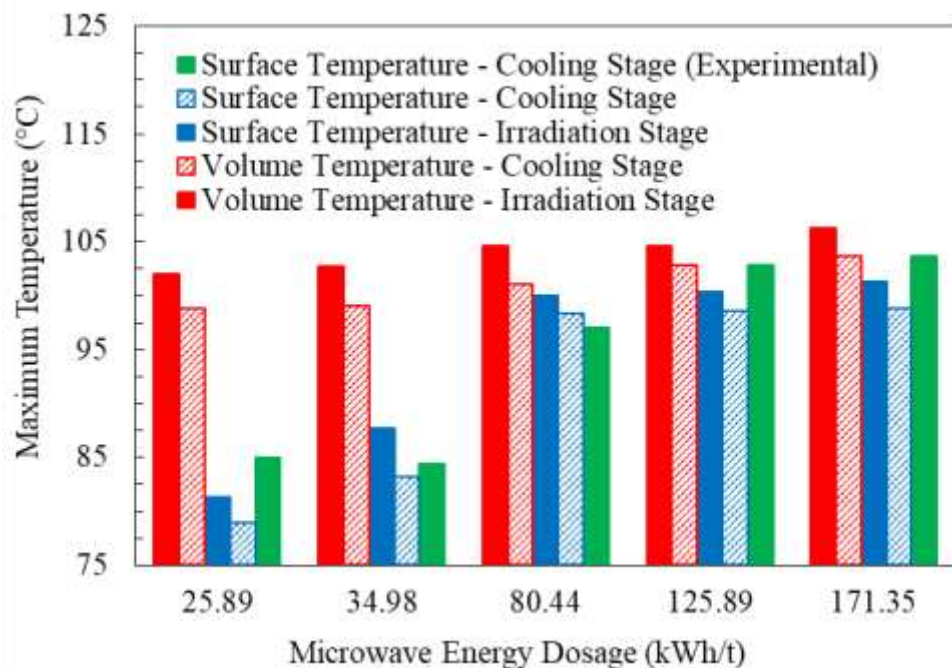


**Figure 3.20** Comparison of maximum surface and volume temperatures. Numerical results for  $\Delta T = 2.5 \text{ }^{\circ}\text{C}$  and  $k_s = 1.79 \text{ W/m.K}$ .

### **3.5 Chapter Conclusion**

This research examined the potential of microwave heating as an innovative alternative to traditional drying methods for sulphur-bearing mineral materials. A comprehensive experimental program, supported by numerical modeling, was undertaken to evaluate its effectiveness in moisture removal. The material underwent extensive characterization, including measurements of thermal conductivity, specific heat capacity, initial moisture content, density, porosity, and dielectric loss factors, to ensure accurate representation in the analysis. Prior to the experimental trials, the microwave oven was carefully inspected to assess its ramp-up performance and quantify the delivered forward power.

To simulate the drying process, a quasi-transient, loosely coupled sequential finite element model was developed to capture the electromagnetic heating dynamics. The model's predictions were systematically compared with experimental data to validate its accuracy. Experimental results indicated that increasing the applied microwave energy dosage significantly improved moisture removal rates. Within the evaporation-dominant drying stage, a steady moisture extraction rate of approximately 0.25 grams per kW.hr/t was recorded. These findings were supported by numerical simulations, which further predicted that the average surface temperature of the samples remained below 100 °C throughout the process. Importantly, the model confirmed that the peak internal temperature did not exceed the industry-recommended maximum of 120 °C, thereby mitigating the risk of unwanted sulphur-related phase changes.

The close agreement between experimental results and numerical predictions was credited to the precise characterization of moisture-dependent material properties and their integration into the computational model. Collectively, the experimental and modeling outcomes demonstrate that microwave drying represents a viable and efficient method for processing temperature-sensitive

minerals. This approach offers significant advantages over conventional kiln-based drying, including better temperature control, reduced risk of hazardous phase transformations, and potential improvements in energy efficiency. These findings suggest that microwave-assisted drying could become a practical and safer alternative for mineral processing applications, enhancing both operational performance and process safety.

## **Chapter 4: Conclusion**

### **4.1 Summary**

This thesis investigated the feasibility of microwave heating as an efficient and sustainable method for drying mineral materials, particularly those containing sulfur. To establish a solid basis for the study, detailed physical and thermal characterizations of the samples were carried out. Properties such as thermal conductivity, heat capacity, density, porosity, moisture content, and dielectric behavior—especially the loss factor that dictates microwave absorption—were measured to predict how the materials would interact with electromagnetic radiation. These data formed the foundation for both the experimental program and the computational modeling.

Drying trials were performed using a calibrated commercial microwave oven. Careful attention was given to quantifying the ramp-up power characteristics and the actual energy delivered to the material, ensuring accuracy and reproducibility of results. In parallel, a finite element simulation framework was developed to model coupled electromagnetic and thermal responses. By incorporating experimentally determined material properties, the model enabled prediction of temperature profiles and moisture transport during heating. Comparison with experimental outcomes provided an opportunity to test the model's robustness, highlight areas of strong agreement, and identify discrepancies caused by simplifying assumptions.

The results consistently indicated that microwave-assisted drying offers clear advantages over conventional thermal techniques. Because microwave energy interacts primarily with water molecules rather than the mineral matrix, the process achieved selective and uniform moisture removal while minimizing excessive heating of the solid phase. Experimental observations confirmed effective drying at controlled temperatures, while numerical predictions supported these

findings and further revealed internal temperature dynamics that are challenging to measure directly with sensors. Importantly, the simulations demonstrated that internal temperatures remained within safe limits, reducing the risk of undesirable sulfur-related transformations.

From an application standpoint, the findings suggest microwave drying could be adopted in mineral processing facilities to improve throughput, reduce energy consumption, and minimize the risks associated with traditional kiln operations. Its potential benefits are particularly relevant for temperature-sensitive ores where conventional heating poses safety or quality challenges.

## 4.2 Objectives, Strength and Limitations

In relation to the thesis **objectives**:

the research successfully showed that microwave heating is not only a technically viable option for mineral drying but also a method with substantial industrial promise. Its contributions lie in validating a combined experimental–numerical approach, advancing understanding of microwave–mineral interactions, and highlighting the method’s potential to enhance both energy efficiency and process safety.

Several **strengths** underpin this work:

the rigorous characterization of moisture-dependent material properties, the careful calibration of experimental systems, and the integration of modeling with empirical validation.

Nonetheless, **limitations** should also be acknowledged.

The study relied on a commercial microwave oven rather than an industrial-scale unit, which may restrict direct scalability. Additionally, the model employed certain

assumptions that, while necessary for tractability, may have excluded secondary effects such as complex chemical transformations or nonuniform moisture redistribution.

### **4.3 Possible Future Research Directions**

Looking ahead, several avenues for future research emerge. Scaling up experiments to pilot or industrial levels would provide insights into energy efficiency under real operating conditions. Further refinement of numerical models to account for evolving porosity or chemical changes could improve predictive accuracy. Exploring hybrid systems that combine microwave energy with conventional heating might also optimize efficiency and cost-effectiveness. Finally, applying the methodology to a broader range of mineral types would establish the versatility and generalizability of the approach across the mining industry.

## Bibliography

1. Cox, B., et al., *The mining industry as a net beneficiary of a global tax on carbon emissions*. Communications Earth & Environment, 2022. **3**(1): p. 17.
2. Akhmat, G., et al., *The challenges of reducing greenhouse gas emissions and air pollution through energy sources: evidence from a panel of developed countries*. Environmental Science and Pollution Research, 2014. **21**(12): p. 7425–7435.
3. Chaedir, B.A., et al., *Advances in dewatering and drying in mineral processing*. Drying Technology, 2021. **39**(11): p. 1667–1684.
4. Norgate, T. and N. Haque, *Energy and greenhouse gas impacts of mining and mineral processing operations*. Journal of Cleaner Production, 2010. **18**(3): p. 266–274.
5. Durgut, E., *Evaluation of the use of microwave energy on green floor/wall tile drying process*. Drying Technology: p. 1–12.
6. Igogo, T., et al., *Integrating renewable energy into mining operations: Opportunities, challenges, and enabling approaches*. Applied Energy, 2021. **300**: p. 117375.
7. Frakos, P., et al., *Energy system transitions and low-carbon pathways in Australia, Brazil, Canada, China, EU-28, India, Indonesia, Japan, Republic of Korea, Russia and the United States*. Energy, 2021. **216**: p. 119385.
8. Rattanadecho, P. and N. and Makul, *Microwave-Assisted Drying: A Review of the State-of-the-Art*. Drying Technology, 2016. **34**(1): p. 1–38.
9. Meloni, E., G. Iervolino, and V. Palma, *Basics of Microwave Heating and Recent Advances*, in *Advances in Microwave-assisted Heterogeneous Catalysis*, J. Hu and B.M. Reddy, Editors. 2023, Royal Society of Chemistry. p. 0.
10. Kingman, S.W., G.M. Corfield, and N.A. Rowson, *Effects of Microwave Radiation Upon the Mineralogy and Magnetic Processing of a Massive Norwegian Ilmenite Ore*. Physical Separation in Science and Engineering, 1999. **9**(3): p. 057075.
11. Galema, S.A., *Microwave chemistry*. Chemical Society Reviews, 1997. **26**(3): p. 233–238.
12. Chen, T.T., et al., *The Relative Transparency of Minerals to Microwave Radiation*. Canadian Metallurgical Quarterly, 1984. **23**(3): p. 349–351.
13. Walkiewicz, J.W., G. Kazonich, and S.L. McGill, *Microwave heating characteristics of selected minerals and compounds*. Minerals & Metallurgical Processing, 1988. **5**(1): p. 39–42.
14. Turner, I.W. and P.C. and Jolly, *COMBINED MICROWAVE AND CONVECTIVE DRYING OF A POROUS MATERIAL*. Drying Technology, 1991. **9**(5): p. 1209–1269.
15. Vollmer, M., *Physics of the Electromagnetic Spectrum*, in *Electromagnetic Technologies in Food Science*. 2021. p. 1–32.
16. Mello, P.A., J.S. Barin, and R.A. Guarneri, *Chapter 2 - Microwave Heating*, in *Microwave-Assisted Sample Preparation for Trace Element Analysis*, É.M.d.M. Flores, Editor. 2014, Elsevier: Amsterdam. p. 59–75.
17. Yoshikawa, N., *Recent Studies on Fundamentals and Application of Microwave Processing of Materials*, in *Advances in Induction and Microwave Heating of Mineral and Organic Materials*, S.T. Grundas, Editor. 2011, IntechOpen: London.
18. Chen, J., et al., *Microwave Treatment of Minerals and Ores: Heating Behaviors, Applications, and Future Directions*. Minerals, 2024. **14**(3): p. 219.

19. Sun, J., W. Wang, and Q. Yue, *Review on Microwave-Matter Interaction Fundamentals and Efficient Microwave-Associated Heating Strategies*. Materials, 2016. **9**(4): p. 231.
20. Mingos, D.M.P. and D.R. Baghurst, *Tilden Lecture. Applications of microwave dielectric heating effects to synthetic problems in chemistry*. Chemical Society Reviews, 1991. **20**(1): p. 1–47.
21. Thostenson, E.T. and T.W. Chou, *Microwave processing: fundamentals and applications*. Composites Part A: Applied Science and Manufacturing, 1999. **30**(9): p. 1055–1071.
22. Huang, J., et al., *A coupled electromagnetic irradiation, heat and mass transfer model for microwave heating and its numerical simulation on coal*. Fuel Processing Technology, 2018. **177**: p. 237–245.
23. Marland, S., A. Merchant, and N. Rowson, *Dielectric properties of coal*. Fuel, 2001. **80**(13): p. 1839–1849.
24. Lester, E. and S. Kingman, *The effect of microwave pre-heating on five different coals*. Fuel, 2004. **83**(14): p. 1941–1947.
25. Lester, E. and S. Kingman, *Effect of Microwave Heating on the Physical and Petrographic Characteristics of a U.K. Coal*. Energy & Fuels, 2004. **18**(1): p. 140–147.
26. Song, Z., et al., *Microwave drying performance of single-particle coal slime and energy consumption analyses*. Fuel Processing Technology, 2016. **143**: p. 69–78.
27. Ge, L., et al., *The interaction between microwave and coal: A discussion on the state-of-the-art*. Fuel, 2022. **314**: p. 123140.
28. Peng, Z., et al., *Dielectric characterization of Indonesian low-rank coal for microwave processing*. Fuel Processing Technology, 2017. **156**: p. 171–177.
29. Tahmasebi, A., et al., *Experimental study on microwave drying of Chinese and Indonesian low-rank coals*. Fuel Processing Technology, 2011. **92**(10): p. 1821–1829.
30. Si, C., et al., *Experimental and numerical simulation of drying of lignite in a microwave-assisted fluidized bed*. Fuel, 2019. **242**: p. 149–159.
31. Fu, B.A., M.Q. Chen, and J.J. Song, *Investigation on the microwave drying kinetics and pumping phenomenon of lignite spheres*. Applied Thermal Engineering, 2017. **124**: p. 371–380.
32. Song, Z., et al., *Experimental Study on the Characteristics of Ignition during Microwave Drying of Lignite*. Energy Technology, 2016. **4**(9): p. 1077–1083.
33. Si, C., et al., *Experimental study on three-stage microwave-assisted fluidized bed drying of Shengli lump lignite*. Drying Technology, 2016. **34**(6): p. 685–691.
34. Sahyoun, C., S.W. Kingman, and N.A. Rowson, *The Effect of Heat Treatment on Chalcopyrite*. Physical Separation in Science and Engineering, 2003. **12**(1): p. 360951.
35. Yang, K., et al., *Microwave roasting and leaching of an oxide-sulphide zinc ore*. Hydrometallurgy, 2016. **166**: p. 243–251.
36. Li, K., et al., *Microwave dielectric properties and thermochemical characteristics of the mixtures of walnut shell and manganese ore*. Bioresource Technology, 2019. **286**: p. 121381.
37. Ling, Y., et al., *Drying kinetics and microstructure evolution of nano-zirconia under microwave pretreatment*. Ceramics International, 2021. **47**(16): p. 22530–22539.
38. Kowalski, S.J. and B. and Mierniczuk, *Analysis of Effectiveness and Stress Development during Convective and Microwave Drying*. Drying Technology, 2007. **26**(1): p. 64–77.

39. Hassini, L., R. Peczalski, and J.-L. Gelet, *Drying of granular medium by hot air and microwaves. Modeling and prediction of internal gas pressure and binder distribution*. Powder Technology, 2015. **286**: p. 636–644.
40. Suwannapum, N. and P. and Rattanadecho, *Analysis of Heat–Mass Transport and Pressure Buildup Induced inside Unsaturated Porous Media Subjected to Microwave Energy Using a Single (TE10) Mode Cavity*. Drying Technology, 2011. **29**(9): p. 1010–1024.
41. Li, K., et al., *Investigations on the microwave absorption properties and thermal behavior of vanadium slag: Improvement in microwave oxidation roasting for recycling vanadium and chromium*. Journal of Hazardous Materials, 2020. **395**: p. 122698.
42. Lou, B., et al., *Microwave heating properties of steel slag asphalt mixture using a coupled electromagnetic and heat transfer model*. Construction and Building Materials, 2021. **291**: p. 123248.
43. Steger, H.F., E. Mark, and L.E. Desiardins, *The drying of sulphide-bearing materials in a microwave oven: A caveat*. Talanta, 1978. **25**(3): p. 181–182.
44. Pitchai, K., et al., *Coupled electromagnetic and heat transfer model for microwave heating in domestic ovens*. Journal of Food Engineering, 2012. **112**(1): p. 100–111.
45. Moyne, C. and P. and Perre, *PROCESSES RELATED TO DRYING: PART I, THEORETICAL MODEL*. Drying Technology, 1991. **9**(5): p. 1135–1152.
46. Perre, P. and C. and Moyne, *PROCESSES RELATED TO DRYING: PART II USE OF THE SAME MODEL TO SOLVE TRANSFERS BOTH IN SATURATED AND UNSATURATED POROUS MEDIA*. Drying Technology, 1991. **9**(5): p. 1153–1179.
47. Kowalski, S.J., R. Kinga, and A. and Rybicki, *Stresses Generated During Convective and Microwave Drying*. Drying Technology, 2005. **23**(9–11): p. 1875–1893.
48. Constant, T., C. Moyne, and P. Perré, *Drying with internal heat generation: Theoretical aspects and application to microwave heating*. AIChE Journal, 1996. **42**(2): p. 359–368.
49. Hassini, L., P. Roman, and J.-L. and Gelet, *Combined Convective and Microwave Drying of Agglomerated Sand: Internal Transfer Modeling with the Gas Pressure Effect*. Drying Technology, 2013. **31**(8): p. 898–904.
50. Kumar, C., et al., *Temperature Redistribution Modelling During Intermittent Microwave Convective Heating*. Procedia Engineering, 2014. **90**: p. 544–549.
51. Li, H., et al., *Pore structure and multifractal analysis of coal subjected to microwave heating*. Powder Technology, 2019. **346**: p. 97–108.
52. Lu, J., et al., *Thermodynamic analysis of moist coal during microwave heating using coupled electromagnetic, multi-phase heat and mass transfer model*. Chemical Engineering Science, 2022. **255**: p. 117690.
53. Lin, B., et al., *Sensitivity analysis on the microwave heating of coal: A coupled electromagnetic and heat transfer model*. Applied Thermal Engineering, 2017. **126**: p. 949–962.
54. Cherbański, R., *Numerical study of heat and mass transfer in the microwave-assisted and conventional packed bed reactors with an irreversible first-order endothermic chemical reaction*. Chemical Engineering and Processing: Process Intensification, 2014. **86**: p. 104–115.
55. Hong, Y.-d., et al., *Three-dimensional simulation of microwave heating coal sample with varying parameters*. Applied Thermal Engineering, 2016. **93**: p. 1145–1154.

56. Li, H., et al., *A fully coupled electromagnetic, heat transfer and multiphase porous media model for microwave heating of coal*. Fuel Processing Technology, 2019. **189**: p. 49–61.
57. Montienthong, P., P. Rattanadecho, and W. Klinbun, *Effect of electromagnetic field on distribution of temperature, velocity and concentration during saturated flow in porous media based on Local Thermal Non-Equilibrium models (influent of input power and input velocity)*. International Journal of Heat and Mass Transfer, 2017. **106**: p. 720–730.
58. Kowalski, S.J., G. Musielak, and J. Banaszak, *Heat and mass transfer during microwave-convective drying*. AIChE Journal, 2010. **56**(1): p. 24–35.
59. Khansary, M.A., et al. *Experimental Evaluation of Microwave Systems for Minerals Dewatering*. 2025. Cham: Springer Nature Switzerland.
60. Travis, K.P., B.D. Todd, and D.J. Evans, *Departure from Navier-Stokes hydrodynamics in confined liquids*. Physical Review E, 1997. **55**(4): p. 4288–4295.
61. Travis, K.P. and K.E. Gubbins, *Poiseuille flow of Lennard-Jones fluids in narrow slit pores*. The Journal of Chemical Physics, 2000. **112**(4): p. 1984–1994.
62. Travis, K.P., B.D. Todd, and D.J. Evans, *Poiseuille flow of molecular fluids*. Physica A: Statistical Mechanics and its Applications, 1997. **240**(1): p. 315–327.
63. Di Marco, P., *The Use of Electric Force as a Replacement of Buoyancy in Two-phase Flow*. Microgravity Science and Technology, 2012. **24**(3): p. 215–228.
64. Kainikkara, M.A., D.S. Pillai, and K.C. Sahu, *Equivalence of sessile droplet dynamics under periodic and steady electric fields*. npj Microgravity, 2021. **7**(1): p. 47.
65. Garivalis, A.I., et al., *Experimental study on evaporation of droplets in microgravity and in the presence of electric field*. Journal of Physics: Conference Series, 2022. **2177**(1): p. 012047.
66. Jeon, D., Y. Kang, and T. Kim, *Observing the Layer-Number-Dependent Local Dielectric Response of WSe<sub>2</sub> by Electrostatic Force Microscopy*. The Journal of Physical Chemistry Letters, 2020. **11**(16): p. 6684–6690.
67. Vernier, P.J., *Dielectric response near an interface—significance of a local dielectric response*. Thin Solid Films, 1981. **82**(1): p. 33–43.
68. Ge, X. and D. Lu, *Local representation of the electronic dielectric response function*. Physical Review B, 2015. **92**(24): p. 241107.
69. Podryabinkin, E.V., et al., *Nanohardness from First Principles with Active Learning on Atomic Environments*. Journal of Chemical Theory and Computation, 2022. **18**(2): p. 1109–1121.
70. Kaatze, U., *Complex permittivity of water as a function of frequency and temperature*. Journal of Chemical & Engineering Data, 1989. **34**(4): p. 371–374.
71. Bergman, D.J., *The dielectric constant of a composite material—A problem in classical physics*. Physics Reports, 1978. **43**(9): p. 377–407.
72. Titulaer, U.M. and J.M. Deutch, *Space and time dependent polarization fluctuations in dielectric media*. The Journal of Chemical Physics, 1974. **60**(7): p. 2703–2713.
73. Booth, F., *The Dielectric Constant of Water and the Saturation Effect*. The Journal of Chemical Physics, 1951. **19**(4): p. 391–394.
74. Fu, B.A., et al., *Non-equilibrium thermodynamics approach for the coupled heat and mass transfer in microwave drying of compressed lignite sphere*. Applied Thermal Engineering, 2018. **133**: p. 237–247.

75. ASTM, *ASTM D5334-22: Standard Test Method for Determination of Thermal Conductivity of Soil and Rock by Thermal Needle Probe Procedure*, in 10.1520/D5334-22. 2022.
76. Höhne, G.W.H., W.F. Hemminger, and H.-J. Flammersheim, *Types of Differential Scanning Calorimeters and Modes of Operation*, in *Differential Scanning Calorimetry*. 2003, Springer Berlin Heidelberg: Berlin, Heidelberg. p. 9–30.
77. Hutcheon, R., M.d. Jong, and F. Adams, *A System for Rapid Measurements of RF and Microwave Properties Up to 1400°C. Part1: Theoretical Development of the Cavity Frequency-Shift Data Analysis Equations*. Journal of Microwave Power and Electromagnetic Energy, 1992. **27**(2): p. 87–92.
78. Hutcheon, R., et al., *A System for Rapid Measurements of RF and Microwave Properties Up to 1400°C. Part 2: Description of Apparatus, Data Collection Techniques and Measurements on Selected Materials*. Journal of Microwave Power and Electromagnetic Energy, 1992. **27**(2): p. 93–102.
79. Nelson, S.O. and S. Trabelsi, *Principles for Microwave Moisture and Density Measurement in Grain and Seed*. Journal of Microwave Power and Electromagnetic Energy, 2004. **39**(2): p. 107–117.
80. Commission, I.E., *Household microwave ovens-Methods for measuring performance*. 2014, International Electrotechnical Commission.
81. Committee, B., *ASTM B962-17 Standard Test Methods for Density of Compacted or Sintered Powder Metallurgy (PM) Products Using Archimedes Principle*. ASTM International, nd <https://doi.org/10.1520/B0962-17>, 2017.
82. Wilson, R.M., *Archimedes's principle gets updated*. Physics Today, 2012. **65**(9): p. 15–17.
83. Nakanishi, K., *Porosity Measurement*, in *Handbook of Sol-Gel Science and Technology: Processing, Characterization and Applications*, L. Klein, M. Aparicio, and A. Jitianu, Editors. 2018, Springer International Publishing: Cham. p. 1399–1409.
84. Brigaud, F. and G. Vasseur, *Mineralogy, porosity and fluid control on thermal conductivity of sedimentary rocks*. Geophysical Journal International, 1989. **98**(3): p. 525–542.
85. Abbasy, F., *Thermal conductivity of mine backfill*, in *Building, Civil and Environmental Engineering*. 2009, Concordia University.
86. Côté, J. and J.-M. Konrad, *A generalized thermal conductivity model for soils and construction materials*. Canadian Geotechnical Journal, 2005. **42**(2): p. 443–458.
87. Zhang, M., et al., *Evaluation of calculation models for the thermal conductivity of soils*. International Communications in Heat and Mass Transfer, 2018. **94**: p. 14–23.
88. Woodside, W. and J.H. Messmer, *Thermal Conductivity of Porous Media. I. Unconsolidated Sands*. Journal of Applied Physics, 1961. **32**(9): p. 1688–1699.
89. Basak, T. and A. Meenakshi, *Influence of ceramic supports on microwave heating for composite dielectric food slabs*. AIChE Journal, 2006. **52**(6): p. 1995–2007.
90. Li, Z.Y., W.R. F., and T. and Kudra, *Uniformity Issue in Microwave Drying*. Drying Technology, 2011. **29**(6): p. 652–660.
91. Idris, A., K. Khalid, and W. Omar, *Drying of silica sludge using microwave heating*. Applied Thermal Engineering, 2004. **24**(5): p. 905–918.

92. Anilkumar, P., P. Dobbidi, and T. and Tiwari, *Historical Developments and Recent Advances in High-power Magnetron: A Review*. IETE Technical Review, 2022. **39**(6): p. 1309–1323.
93. Canada, S.C.o., *Household microwave ovens - Methods for measuring performance*.
94. Vasilakos, N.P. and F. and Magalhaes, *Microwave Drying of Polymers*. Journal of Microwave Power, 1984. **19**(2): p. 135–144.
95. Liu, C.-l., et al., *Numerical study on the temporal variations and physics of heat transfer coefficient on a flat plate with unsteady thermal boundary conditions*. International Journal of Thermal Sciences, 2017. **113**: p. 20–37.
96. Mishra, R.R. and A.K. Sharma, *Microwave–material interaction phenomena: Heating mechanisms, challenges and opportunities in material processing*. Composites Part A: Applied Science and Manufacturing, 2016. **81**: p. 78–97.
97. Alam, T.-M. and L. Paquet, *The coupled heat Maxwell equations with temperature-dependent permittivity*. Journal of Mathematical Analysis and Applications, 2022. **505**(1): p. 125472.
98. Sadeghi, G., *Energy storage on demand: Thermal energy storage development, materials, design, and integration challenges*. Energy Storage Materials, 2022. **46**: p. 192–222.
99. Jin, J.M. and S. Yan, *Multiphysics Modeling in Electromagnetics: Technical Challenges and Potential Solutions*. IEEE Antennas and Propagation Magazine, 2019. **61**(2): p. 14–26.
100. COMSOL Multiphysics® v. 6.3 COMSOL AB: Stockholm, Sweden.
101. Tretyakov, S., *Analytical Modeling in Applied Electromagnetics*. 2003: Artech House.
102. Dibben, D.C. and N. Metaxas, *Frequency domain vs. time domain finite element methods for calculation of fields in multimode cavities*. IEEE Transactions on Magnetics, 1997. **33**(2): p. 1468–1471.
103. Acharya, R., *Chapter 2 - Maxwell's equation and EM waves*, in *Satellite Signal Propagation, Impairments and Mitigation*, R. Acharya, Editor. 2017, Academic Press. p. 27–56.
104. Raabe, G. and R.J. Sadus, *Molecular dynamics simulation of the effect of bond flexibility on the transport properties of water*. J Chem Phys, 2012. **137**(10): p. 104512.
105. Braun, D., S. Boresch, and O. Steinhauser, *Transport and dielectric properties of water and the influence of coarse-graining: comparing BMW, SPC/E, and TIP3P models*. J Chem Phys, 2014. **140**(6): p. 064107.
106. Purdue, M.J., et al., *A comparative study of the properties of polar and nonpolar solvent/solute/polystyrene solutions in microwave fields via molecular dynamics*. J Chem Phys, 2006. **125**(11): p. 114902.
107. Bur, A.J., *Dielectric properties of polymers at microwave frequencies: a review*. Polymer, 1985. **26**(7): p. 963–977.
108. Forsh, P.A., et al., *Mobility of charge carriers in porous silicon layers*. Journal of Experimental and Theoretical Physics, 2009. **107**(6): p. 1022–1026.
109. He, W., et al., *Reconstructing charge-carrier dynamics in porous silicon membranes from time-resolved interferometric measurements*. Sci Rep, 2018. **8**(1): p. 17172.
110. Hyun, G., et al., *Three-Dimensional, Submicron Porous Electrode with a Density Gradient to Enhance Charge Carrier Transport*. ACS Nano, 2022. **16**(6): p. 9762–9771.

111. Zhang, H.T., T. Zhang, and X. Zhang, *Perspective and Prospects for Ordered Functional Materials*. Adv Sci (Weinh), 2023. **10**(13): p. e2300193.
112. Boyd, R.W., *Order-of-magnitude estimates of the nonlinear optical susceptibility*. Journal of Modern Optics, 1999. **46**(3): p. 367–378.
113. Boyd, R.W., *Chapter 1 - The Nonlinear Optical Susceptibility*, in *Nonlinear Optics (Third Edition)*, R.W. Boyd, Editor. 2008, Academic Press: Burlington. p. 1–67.
114. Ayappa, K.G., et al., *Microwave heating: an evaluation of power formulations*. Chemical Engineering Science, 1991. **46**(4): p. 1005–1016.
115. Sumnu, G. and S. Sahin, *16 - Recent Developments in Microwave Heating*, in *Emerging Technologies for Food Processing*, D.-W. Sun, Editor. 2005, Academic Press: London. p. 419–444.
116. Remsburg, R., *Heat Transfer With Phase Change*, in *Advanced Thermal Design of Electronic Equipment*. 1998, Springer US: Boston, MA. p. 437–498.
117. Pena, F.J.C. and M.J.S. de Lemos, *Unsteady heat conduction with phase change applied to a novel thermal plug and abandonment process*. International Journal of Thermal Sciences, 2021. **170**: p. 107155.
118. Yang, G., A.D. Migone, and K.W. Johnson, *Heat capacity and thermal diffusivity of a glass sample*. Physical Review B, 1992. **45**(1): p. 157–160.
119. Halder, A. and A.K. Datta, *Surface heat and mass transfer coefficients for multiphase porous media transport models with rapid evaporation*. Food and Bioproducts Processing, 2012. **90**(3): p. 475–490.
120. Osczevski, R.J., *The basis of wind chill*. Arctic, 1995: p. 372–382.
121. Salvi, D., et al., *COMSOL Multiphysics model for continuous flow microwave heating of liquids*. Journal of Food Engineering, 2011. **104**(3): p. 422–429.
122. Zhang, H., et al., *Electromagnetics, heat transfer, and thermokinetics in microwave sterilization*. AIChE Journal, 2001. **47**(9): p. 1957–1968.
123. de Moura, C.A. and C.S. Kubrusly, *The Courant–Friedrichs–Lewy (CFL) Condition: 80 Years After Its Discovery*. 2012: Birkhäuser Boston.
124. Kelley, C.T. and D.E. Keyes, *Convergence Analysis of Pseudo-Transient Continuation*. SIAM Journal on Numerical Analysis, 1998. **35**(2): p. 508–523.
125. Lobo, M. and A.F. and Emery, *USE OF THE DISCRETE MAXIMUM PRINCIPLE IN FINITE-ELEMENT ANALYSIS OF COMBINED CONDUCTION AND RADIATION IN NONPARTICIPATING MEDIA*. Numerical Heat Transfer, Part B: Fundamentals, 1995. **27**(4): p. 447–465.
126. Fachinotti, V.D. and M. Bellet, *Linear tetrahedral finite elements for thermal shock problems*. International Journal of Numerical Methods for Heat & Fluid Flow, 2006. **16**(5): p. 590–601.
127. Reddy, J.N., *CHAPTER PRELIMINARIES*, in *Introduction to the Finite Element Method, Third Edition*. 2006, McGraw-Hill Education: New York.
128. Kittur, M.G. and R.L. Huston, *Mesh refinement in finite element analysis by minimization of the stiffness matrix trace*. 1989, Lewis Research Center, National Aeronautics and Space Administration (NASA).
129. Arballo, J.R., S.M. Goñi, and R.H. Mascheroni, *Modeling of fluid dynamics and water vapor transport in microwave ovens*. Food and Bioproducts Processing, 2020. **119**: p. 75–87.

130. Essen, L. and K.D. Froome, *The Refractive Indices and Dielectric Constants of Air and its Principal Constituents at 24,000 Mc/s*. Proceedings of the Physical Society. Section B, 1951. **64**(10): p. 862.
131. Kui, J., *Microwave Dielectric Ceramic Materials and Their Industry Development Overview and Future Prospects*. Journal of Physics: Conference Series, 2021. **1885**(3): p. 032034.
132. Geedipalli, S.S.R., V. Rakesh, and A.K. Datta, *Modeling the heating uniformity contributed by a rotating turntable in microwave ovens*. Journal of Food Engineering, 2007. **82**(3): p. 359–368.
133. Tubini, N., S. Gruber, and R. Rigon, *A method for solving heat transfer with phase change in ice or soil that allows for large time steps while guaranteeing energy conservation*. The Cryosphere, 2021. **15**(6): p. 2541–2568.
134. Khattari, Y., et al., *Apparent heat capacity method to investigate heat transfer in a composite phase change material*. Journal of Energy Storage, 2020. **28**: p. 101239.
135. Vermeer, P.A. and A. Verruijt, *An accuracy condition for consolidation by finite elements*. International Journal for Numerical and Analytical Methods in Geomechanics, 1981. **5**(1): p. 1–14.
136. Fei, W., G.A. Narsilio, and M.M. Disfani, *Impact of three-dimensional sphericity and roundness on heat transfer in granular materials*. Powder Technology, 2019. **355**: p. 770–781.
137. King, A.P. and R.J. Eckersley, *Chapter 1 - Descriptive Statistics I: Univariate Statistics*, in *Statistics for Biomedical Engineers and Scientists*, A.P. King and R.J. Eckersley, Editors. 2019, Academic Press. p. 1–21.
138. Kemp, I.C., *Fundamentals of Energy Analysis of Dryers*, in *Modern Drying Technology*. 2011. p. 1–45.
139. Jindarat, W., P. Rattanadecho, and S. Vongpradubchai, *Analysis of energy consumption in microwave and convective drying process of multi-layered porous material inside a rectangular wave guide*. Experimental Thermal and Fluid Science, 2011. **35**(4): p. 728–737.
140. Hassani, F., et al., *Energy analysis of the effectiveness of microwave-assisted fragmentation*. Minerals Engineering, 2020. **159**: p. 106642.